Journal of Climate

GFDL's ESM2 global coupled climate-carbon Earth System Models Part I: Physical formulation and baseline simulation characteristics

--Manuscript Draft--

Manuscript Number:	
Full Title:	GFDL's ESM2 global coupled climate-carbon Earth System Models Part I: Physical formulation and baseline simulation characteristics
Article Type:	Article
Corresponding Author:	John Patrick Dunne, Ph D. National Oceanic and Atmospheric Administration Princeton, NJ UNITED STATES
Corresponding Author's Institution:	National Oceanic and Atmospheric Administration
First Author:	John Patrick Dunne, Ph D.
All Authors:	John Patrick Dunne, Ph D.
	Jasmin G John
	Alistair J Adcroft
	Stephen M Griffies
	Robert W Hallberg
	Elena N Shevliakova
	Ronald J Stouffer
	William Cooke
	Krista A Dunne
	Matthew J Harrison
	John P Krasting
	Hiram Levy
	Sergey L Maleshev
	P C. D. Milly
	Peter J. Phillipps
	Lori A Sentman
	Bonita L. Samuels
	Michael J Spelman
	Michael Winton
	Andrew T. Wittenberg
	Niki Zadeh
Abstract:	We describe the physical climate formulation and simulation characteristics of two new global coupled carbon-climate Earth System Models, ESM2M and ESM2G. These models demonstrate similar climate fidelity as the Geophysical Fluid Dynamics Laboratory's previous CM2.1 climate model while incorporating explicit and consistent carbon dynamics. The two models differ exclusively in the physical ocean component; ESM2M uses Modular Ocean Model version 4.1 with vertical pressure layers while ESM2G uses Generalized Ocean Layer Dynamics with a bulk mixed layer and interior isopycnal layers. Differences in the ocean mean state include the thermocline depth being relatively deep in ESM2M and relatively shallow in ESM2G compared to observations. The crucial role of ocean dynamics on climate variability is highlighted in the El Nino Southern Oscillation being overly strong in ESM2M and overly weak

Powered by Editorial Manager® and Preprint Manager® from Aries Systems Corporation

	the El Nino Southern Oscillation being overly strong in ESM2M and overly weak ESM2G relative to observations. The major advantages of ESM2G over ESM2M are representation of: channels and topography, water mass properties in overflows and deep waters, and convection in the Northwest Pacific. The major advantages of ESM2M over ESM2G are representation of: sea surface temperature and salinity in the Southern Ocean and Equatorial Pacific, and Southern Ocean mixed layers and interior salinity structure. Our overall assessment is that neither model is fundamentally superior to the other, and that both models achieve sufficient fidelity to allow meaningful climate and earth system modeling applications. This affords us the unique ability to assess the role of ocean configuration on earth system interactions in the context of two state of the art coupled carbon-climate models.
Suggested Reviewers:	Jonathan Gregory j.m.gregory@reading.ac.uk
	Chris Jones chris.d.jones@metoffice.gov.uk
	David Lawrence dlawren@ucar.edu
	Joellen Russell jrussell@email.arizona.edu
	Sandrine Bony sandrine.bony@lmd.jussieu.fr

Powered by Editorial Manager® and Preprint Manager® from Aries Systems Corporation

Cover Letter
Common.Links.ClickHereToDownload

`

UNITED STATES DEPARTMENT OF COMMERCE
National Oceanic and Atmospheric Administration
GEOPHYSICAL FLUID DYNAMICS LABORATORY
Princeton University
Forrestal Campus, US Route 1

September 12, 2011

TO: Dr. Anthony J. Broccoli
Editor, Journal of Climate

SUBJECT: GFDL ESM2M/ESM2G physical documentation manuscript

Dear Dr. Broccoli,

My co-authors and myself a proud to submit for your consideration the manuscript, "GFDL's ESM2 global coupled climate-carbon Earth System Models Part I: Physical formulation and baseline simulation characteristics" which provides the background physical climate description for GFDL's two coupled carbon Earth System Models that are being used as GFDL's contribution in support of the fifth phase of the Coupled Model Intercomparison Project in preparation for the fifth assessment of the Intergovernmental Panel on Climate Change. We plan to submit to you a companion manuscript describing he carbon cycles of these two models within the next month in order to hopefully publish as a set. Together, we believe these manuscripts represent a critical contribution to the climate modeling field as they describe a new set of state of the art coupled carbon climate models and explore the role of ocean physical configuration on climate sensitivity. Thank you very much for your consideration of this manuscript. Please let me know if there is anything I can do to expedite it's consideration.

Sincerely,

John Dunne
Research Oceanographer
NOAA – Geophysical Fluid Dynamics laboratory
(609) 452-6596
email: John.Dunne@noaa.gov

Manuscript (non-LaTeX)
Common.Links.ClickHereToDownload

GFDL's ESM2 global coupled climate-carbon Earth System Models Part I: Physical formulation and baseline simulation characteristics

John P. Dunne[a], Jasmin G. John[a], Alistair J. Adcroft[b], Stephen M. Griffies[a], Robert W. Hallberg[a], Elena N. Shevliakova[c], Ronald J. Stouffer[a], William Cooke[d], Krista A. Dunne[e], Matthew J. Harrison[a], John P. Krasting[d,a], Hiram Levy[a], Sergey L. Malyshev[c], P. C. D. Milly[e], Peter J. Phillipps[a], Lori A. Sentman[a], Bonita L. Samuels[a], Michael J. Spelman[d], Michael Winton[a], Andrew T. Wittenberg[a], Niki Zadeh[d]

[a]National Oceanic and Atmospheric Administration/Geophysical Fluid Dynamics Laboratory, Princeton, New Jersey

[b]Program in Atmospheric and Oceanic Sciences, Princeton University, Princeton, New Jersey

[c]Department of Ecology and Evolutionary Biology, Princeton University, Princeton, New Jersey

[d]High Performance Technologies, Inc./GFDL, Princeton, New jersey.

[e]U.S. Geological Survey, and National Oceanic and Atmospheric Administration/Geophysical Fluid Dynamics Laboratory, Princeton, New Jersey

Draft for submission to the Journal of Climate

September 8, 2011

Abstract

We describe the physical climate formulation and simulation characteristics of two new global coupled carbon-climate Earth System Models, ESM2M and ESM2G. These models demonstrate similar climate fidelity as the Geophysical Fluid Dynamics Laboratory's previous CM2.1 climate model while incorporating explicit and consistent carbon dynamics. The two models differ exclusively in the physical ocean component; ESM2M uses Modular Ocean Model version 4.1 with vertical pressure layers while ESM2G uses Generalized Ocean Layer Dynamics with a bulk mixed layer and interior isopycnal layers. Differences in the ocean mean state include the thermocline depth being relatively deep in ESM2M and relatively shallow in ESM2G compared to observations. The crucial role of ocean dynamics on climate variability is highlighted in the El Nino Southern Oscillation being overly strong in ESM2M and overly weak ESM2G relative to observations. The major advantages of ESM2G over ESM2M are representation of: channels and topography, water mass properties in overflows and deep waters, and convection in the Northwest Pacific. The major advantages of ESM2M over ESM2G are representation of: sea surface temperature and salinity in the Southern Ocean and Equatorial Pacific, and Southern Ocean mixed layers and interior salinity structure. Our overall assessment is that neither model is fundamentally superior to the other, and that both models achieve sufficient fidelity to allow meaningful climate and earth system modeling applications. This affords us the unique ability to assess the role of ocean configuration on earth system interactions in the context of two state of the art coupled carbon-climate models.

Introduction

We describe the physical formulation and simulation characteristics of two new global coupled carbon-climate Earth System Models (ESMs) developed over the last several years at the Geophysical Fluid Dynamics Laboratory (GFDL) of the National Oceanic and Atmospheric Administration (NOAA) to advance understanding of how earth's biogeochemical cycles, including human actions, interact with the climate system. The models are the product of an effort to expand upon the capabilities of past GFDL models used to study climate on seasonal to centennial time scales (e.g., Manabe et al., 1991; Rosati et al., 1997; Delworth et al., 2002; Delworth et al., 2006). Our approach has been to develop two Earth System Models with different ocean dynamical/physical cores while keeping all other components the same. The atmosphere and sea ice components in the new ESMs are very similar to those in GFDL's previous CM2.1 (Delworth et al., 2006). The new land component includes new hydrology, physics and terrestrial ecology components (LM3.0; Milly et al., in preparation). The ocean dynamical/physical component in CM2.1 was replaced by two new ocean components using the same ocean ecology and biogeochemistry – one in which the vertical coordinate is based on depth (ESM2M) and another in which the vertical coordinate is based on density (ESM2G) . These independent frameworks for describing the ocean allow us to explore the sensitivity of ocean response under anthropogenic CO_2 forcing and climate change to ocean configuration. In traditional depth coordinates, the ocean is divided into boxes in which horizontally adjacent pressures interact, typically emphasizing resolution near the sea surface. While this framework holds many benefits, it leads to fundamental problems in representing the lateral connectivity between vertical boxes given their extremely skewed horizontal/vertical aspect ratio and results

in spurious numerical mixing and difficulty in representing bottom-following flows such as dense overflows down topography. An isopycnal framework resolves these problems by taking advantage of the relative ease of motion along isopycnal layers and explicitly characterizing the diapycnal transfer between these layers, but adds its own representational challenges. Comparison between these formulations allows us to assess the relative fidelity of these approaches and reduce uncertainty in the sensitivity of our results to model assumptions.

We built ESM2M and ESM2G specifically to study carbon-climate interactions and feedbacks in the context of global climate change under the influence of increase greenhouse gases. Results obtained from these model integrations will be part of the Coupled Model Inter-comparison Project version 5 (Taylor et al. 2011). This paper serves as Part I of two companion papers. Part I documents the physical climate formulation and baseline simulation characteristics of these two ESMs. It also discusses the initialization methods used to obtain stable climate states. Finally it presents a few results from the pre-industrial control integrations (nominally 1860). Part II documents the ecological and biogeochemical formulation and baseline simulation characteristics of these models (Dunne et al., in preparation).

Model description

The physical coupled model (CM2.1) used as the base for these ESMs is documented in Delworth et al. (2006), Gnanadesikan et al. (2006), Griffies et al. (2005), and Anderson et al. (2004). Here, we focus the description on those aspects which are new to ESM2M and ESM2G.

Coupling

The component models pass fluxes across their interfaces using an exchange grid system. The exchange grid enforces energy, mass and tracer conservation on the fluxes passed between the component models. The atmosphere, land, and sea ice radiative components are coupled every 30 minutes. The ocean tracer time step and atmosphere-ocean tracer coupling interval are 2 hours.

Atmosphere

The atmospheric component (AM2) is virtually identical to that in CM2.1, incorporating only a few minor code updates that were found to not appreciably affect climate. AM2 uses a horizontal grid spacing of 2° latitude by 2.5° longitude. There are 24 vertical levels. The atmospheric component uses a D-grid and the advection scheme uses the finite volume technique (Lin, 2004) with a 30 minute dynamical time step and a 3 hour radiation time step to resolve the diurnal cycle. The atmospheric physical parameterizations are described in detail in Anderson et al. (2004). The radiation code and configuration is also unchanged from CM2.1. The orbital parameters are held constant at 1860 values for computation of incoming solar radiation. Radiatively active trace gases and aerosols are also held constant at 1860 values after Delworth et al. (2006). Three-dimensional, time mean distributions of aerosols (i.e. black carbon, organic carbon, sulfates, dust, sea salt, volcanoes) are specified as input concentration fields.

Land

The land model in both ESMs (LM3.0) is described in Milly et al. (in preparation) and Donner et al. (2011) representing land water, energy, and carbon cycles. LM3.0 includes a multi-layer model of snow pack above the soil; continuous vertical representation of soil water spanning both the unsaturated and saturated zones; a frozen soil-water phase; parameterization of water-table height, saturated-area fraction, and groundwater discharge to streams derived from standard groundwater-hydraulic assumptions and surface topographic information; finite-velocity horizontal transport of runoff via rivers to the ocean; lakes, lake ice, and lake-ice snow packs that exchange mass and energy with both the atmosphere and the rivers; consistent, energy-conserving accounting of sensible heat content of water in all phases. Temperature is tracked in the vegetation canopy, leaves, and in multiple soil/snow layers. Vegetation radiation, hydrology and carbon dynamics are tracked by means of an extension of the model of Shevliakova et al. (2009). For radiative transport, the vegetation canopy is treated as a dispersed medium where leaf reflectance is dependent on leaf properties and amount of intercepted snow. The canopy is underlain by a reflective, opaque surface of soil and/or snow, with extent of snow depending on snow depth. Sufficiently deep snow can mask a fraction of the canopy itself. Bare soil and snow radiation parameters were specified either directly from maps of Moderate Resolution Imaging Spectroradiometer bidirectional reflectance distribution function parameters (MOD43C2 V004; https://lpdaac.usgs.gov/lpdaac/products/modis_products_table/brdf_albedo_snow_free_quality/16_day_l3_global_0_05deg_cmg/mcd43c2; Land Processes Distributed Active Archive Center (LP DAAC), U.S. Geological Survey (USGS) Earth Resources Observation and Science (EROS) Center (lpdaac.usgs.gov).)

Sea Ice

The sea ice component (Winton, 2000) is very similar to that in CM2.1. It has full ice dynamics, a three-layer thermodynamics (two ice, one snow), and a scheme for tracing 5 different ice thickness categories and open water at each grid point. The sea ice model uses the same tri-polar grid as the ocean component (Murray, 1996) and uses the B-grid spatial discretization of MOM4p1. The ice albedos (snow on ice albedo = 0.85, ice albedo = 0.65 compared to snow on ice albedo = 0.80 and ice albedo = 0.5826 in CM2.1) and temperature range of melting (1°C compared to 10°C in CM2.1) were modified to use values based on observations (Perovich et al., 2002). In addition, a sea ice diffusion parameterization was added for narrow (1-point-wide) channels in ESM2G.

Icebergs

Icebergs are supplied through the ice calving term in LM3.0. Whenever the snow depth in LM3.0 exceeds a critical value, excess snow is transported to the ocean via rivers. This frozen water runoff, a rudimentary representation of land ice calving, is given to the ocean-sea-ice component in coastal cells where it is accumulated and released as icebergs according to a prescribed size distribution. Within the iceberg model, clusters of icebergs are treated as Lagrangian particles of frozen fresh-water with trajectories determined by drag on the icebergs by the atmosphere, ocean, and sea-ice (Martin and Adcroft, 2010). The icebergs impart their weight on the ocean and deposit fresh and 0°C melt water but do not affect the radiation or momentum balance of the ocean, sea-ice or atmosphere.

MOM4p1 (ESM2M Ocean)

The ocean component of ESM2M employs the MOM4p1 code of Griffies (2009) configured with the same horizontal and vertical grid dimensions as the CM2.1 ocean component (Griffies et al., 2005; Gnanadesikan et al., 2006; 1° horizontal grid up to 1/3° meridionally at the equator; 50 vertical levels). ESM2M ocean uses a rescaled geopotential vertical coordinate (z*; Stacey et al., 1995; Adcroft and Campin, 2004) that allows for a more robust treatment of free surface undulations than the traditional depth coordinate. For tracer advection, ESM2M uses the multi-dimensional piecewise parabolic method (MDPPM) ported from the MITgcm (Marshall et al., 1997). In idealized simulations, the MDPPM method was found to be more accurate (less diffusive) than the CM2.1 advection scheme while still preserving monotonicity. Neutral (isopycnal) diffusion is based on Griffies et al. (1998) with constant diffusivity of 600 $m^2 s^{-1}$ and the slope tapering scheme of Danabasoglu and McWilliams (1995) as in CM2.1 but uses a larger value of 1/200 for the maximum slope (Gnanadesikan et al., 2007a) which has been shown to greatly improve the abyssal export of waters out of the Southern Ocean (Downes et al., 2011). For the parameterization of eddies, ESM2M uses the skew flux approach of Griffies (1998) but computes the quasi-Stokes stream function via a boundary value problem extending across the full column after Ferrari et al. (2010) rather than the local approach of Gent and McWilliams (1990) and Gent et al. (1995). As in CM2.1, the horizontal variation of the eddy diffusivity in ESM2M is based on local flow properties (Griffies et al., 2005) but with an expanded allowable range of 100$m^2 s^{-1}$ to 800 $m^2 s^{-1}$. The ESM2M implementation includes updates to the K-profile parameterization (Large et al.,

1994) based on Danabasoglu et al. (2006), as well as model-predicted chlorophyll modulation of shortwave radiation penetration through the water column.

ESM2M also includes completely novel parameterizations relative to CM2.1. Parameterization of sub-mesoscale eddy induced mixed layer re-stratification in ESM2M is implemented according to Fox-Kemper et al. (2011). Instead of the prescribed vertical diffusivity for interior mixing of Bryan and Lewis (1979) used in CM2.1, ESM2M employs the Simmons et al. (2004) scheme along with a depth independent background diffusivity of 1.0 x 10^{-5} m^2 s^{-1} in the tropics and 1.5 x 10^{-5} m^2 s^{-1} poleward of 30° latitude following a tanh curve. ESM2M implements geothermal heating following from the approach of Adcroft et al. (2001). While CM2.1 used the horizontal anisotropic friction scheme from Large et al. (2001), ESM2M uses an isotropic Laplacian friction and a western boundary enhanced biharmonic friction with less frictional dissipation to allow more vigorous tropical instability wave activity at the expense of adding zonal grid noise, particularly in the tropics.

GOLD (ESM2G Ocean)

The ocean component of ESM2G employs the Generalized Ocean Layer Dynamics (GOLD) isopycnal code originally developed by Hallberg (1995) with a 1° horizontal grid up to 1/3° meridionally at the equator. The model includes two mixed layer layers, two buffer layers, and 59 interior layers to provide a reasonable resolution across both the narrow density range of the Southern Ocean and the broad dense-to-light water structure from bottom waters to low latitudes and marginal seas. A three-way barotropic, baroclinic, and diabatic/tracer split time-stepping scheme (Hallberg, 1997; Hallberg and Adcroft, 2009) with sub-cycling of shorter time

steps assures that the model can be integrated efficiently while conserving momentum, mass, tracers, potential vorticity, and energy (Arakawa and Hsu 1990). Monotonic tracer advection is based on Easter (1993). The interior isopycnal layers track prescribed values of potential density with a 2000 dbar reference pressure (Sun et al. 1999; Hallberg, 2000). For all aspects of the dynamics, the full nonlinear equation of state is used. To avoid thermobaric instability arising from the traditional Montgomery potential form of the pressure gradient force (Hallberg 2005), ESM2G uses the analytically integrated finite volume pressure gradient discretization of Adcroft et al. (2008).

Diapycnal diffusivity between interior layers in ESM2G combines multiple parameterizations. The background diapycnal diffusivity is prescribed using the latitude-dependent profile proposed by Henyey et al. (1986) and described in Harrison and Hallberg (2008) of 2×10^{-5} m^2 s^{-1} at 30°N decreasing to a minimum of 2×10^{-6} m^2 s^{-1} at the equator. Turbulent entrainment in descending overflows and other regions of small resolved shear Richardson number is parameterized after Jackson et al. (2006). Additionally, the bottom boundary layer is mixed using the parameterization of Legg et al. (2005), in which 20% of the energy extracted by bottom drag is used to thicken a well-mixed bottom boundary layer. As in ESM2M, ESM2G uses the baroclinic tide mixing of Simmons et al (2004) and geothermal heating based on Adcroft et al. (2001). To maintain the weakly stratified abyss, ESM2G uses a floor on the turbulent dissipation rate of ($\varepsilon_{min}=1.0\times10^{-7}$ m^2 s^{-3} + 6.0×10^{-4} m^2 s^{-2} N), where N is the buoyancy frequency after Gargett (1984) combined with an assumed flux Richardson number of $F_{Ri}=0.2N^2/(N^2+\Omega^2)$ to give a minimum diapycnal diffusivity of $\kappa_{Min}=0.2N^2\varepsilon_{Min}/(N^2+\Omega^2)$.

ESM2G incorporates a bulk mixed layer based on Hallberg (2003) and Thompson et al. (2003) with two additional buffer layers below it for smooth water mass exchange with the isopycnal interior. The mixed layer depth is determined by a turbulent kinetic energy budget after Kraus and Turner (1967). This mixed layer is divided into two layers which are well mixed with respect to tracers but not with respect to velocity. Sub-mesoscale eddy-driven restratification of the mixed layer is parameterized after Fox-Kemper et al. (2010) to avoid mixed layer depths becoming excessively deep (Hallberg, 2003). The two buffer layers allow the mixed layer to retreat and advance with both diurnal and longer timescales without introducing unphysical surface property biases (Hallberg et al., in preparation). Like ESM2M, ESM2G includes dynamic representation of model-predicted chlorophyll modulation of shortwave radiation penetration through the water column. ESM2G uses a thickness diffusion parameterization motivated by Gent and McWilliams (1990) with a local slope-dependent coefficient varying between 10 and 900 $m^2\ s^{-1}$. Dissipation of momentum is implemented with Laplacian and biharmonic viscosities. The Laplacian coefficient is Δx multiplied by 1 cm s^{-1}. The biharmonic viscosity is the larger of Δx^3 multiplied by 5 cm s^{-1} and a Smagorinsky (1993) viscosity with a non-dimensional coefficient of 0.06 (Griffies and Hallberg, 2000).

Initialization

To obtain 1860 initial conditions for ESM control and perturbation integrations, a method similar to that described by Stouffer et al. (2004) is used. The ocean model is initialized with present day ocean temperature (Locarnini et al., 2006) and salinity (Antonov et al., 2006) from the World Ocean Atlas 2005 and run for one year forced by atmospheric conditions from a

CM2.1 1990 control run. The fully coupled models were then integrated over 1000 model years with 1860 solar and radiative forcing before declaring 'quasi steady state equilibrium' and beginning the 1860 control and perturbation integrations. In addition to the many qualitative requirements, we define acceptable 'quasi steady state equilibrium' with quantitative metrics: net top of the atmosphere radiative fluxes less than 0.5 W m^{-2}; surface temperature drifts less than 0.1 °C per century; stable Atlantic Meridional Overturning Circulation above 10 Sv (1 Sv=10^6 m^3 s^{-1}); local sea surface temperature (SST) biases less than ~9°C; global 70°S-70°N root mean square SST errors less than 1.9°C; global net CO_2 fluxes between the atmosphere and both land and ocean lower than 20 PgC per century (averaged over two centuries). For accelerated initialization of the terrestrial soil component, years 551-600 of the integration were used to project equilibrium values offline (Shevliakova et al, 2009).

Results

Here we compare the model control integrations to observations which are mainly taken near present day. We do this knowing that 1860 conditions were likely colder than present day but focus our analysis on those differences that are expected to be larger than the forced climate changes over the last 150 years. We show results averaged over years 1001-1100 of the integrations unless otherwise noted.

Climate drift from present day initialization

When initialized with present day ocean observations and given 1860 radiative forcing, the climate in both models cools (Figure 2). The net radiation at the top of the model

atmosphere (TOA, Figure 2A) and the oceanic heat flux (Figure 2C) become strongly negative (implying cooling of the climate system and the ocean respectively). In response, the surface air temperature (SAT; Figure 2B) and sea surface temperature (SST; Figure 2D) cool in both models by more than 1°C in the first century. In subsequent centuries however, the SAT and SST warm about 0.6°C in ESM2M and 0.3°C in ESM2G. After detrending, the models have similar total inter-annual variability (σ = 0.13°C for both models), with SAT variability largely following SST variability (r^2=0.9 for both models) and ESM2G partitioning more variability into the multi-decadal range.

While the initial evolution of the surface temperature from the present day to 1860 conditions in the two models is quite similar, the overall ocean heat flux and subsequent ocean volume average temperature responses are quite different. In ESM2M, the TOA and oceanic heat flux reverse sign and begin to warm the ocean as a whole after year 11. The long term drift in volume averaged temperature (Figure 2E) is 0.60°C over the 1000 year period. By year 1000, the rate of warming in ESM2M diminishes to 0.038°C century^{-1}. This deep ocean warming phenomenon is common to earlier versions of this model (Delworth et al. 2006) as well as many other atmosphere-ocean models (Randall et al. 2007 Supplemental Material), and tends to occur as a fundamental model drift away from the observed initial condition rather than as a consequence of the particular radiative forcing. In ESM2G, the TOA and ocean surface fluxes gradually approach zero over the first 50 years, but the ocean heat flux remains slightly negative throughout the 1000 year period with the volume averaged temperature (Figure 2E) cooling by 0.18°C. By year 1000, the rate of cooling in ESM2G diminishes to -0.010°C century^{-1}. Both models undergo a spin-up phase of the Atlantic Meridional Overturning Circulation (AMOC)

over the first century followed by a slight drop over the second and third centuries before becoming stable (Figure 2G). After spin-up, AMOC in ESM2M is stronger (28.1 ± 1.8 Sv) than in ESM2G (23.6 ± 1.7 Sv). As was seen for SAT and SST, AMOC variability in ESM2M is characterized by relatively strong, regular 18 year period while that in ESM2G is longer (26 years) and less regular. This highlights the important role of ocean formulation in determining modes of climate variability.

The vertical structure of global ocean temperature drift (Figure 3A) is characterized by a thermocline deepening in ESM2M (red) as it warms over much of the water column relative to present day observations (black) and by thermocline shoaling in ESM2G (green) as the upper 2000 m cools with warming below. Both models warm extensively in the deep Atlantic (Figure 3C) while ESM2M also warms extensively in the Southern Ocean (Figure 3E). In all three oceans, biases and root-mean-square errors in ESM2G are found to be significantly lower than in ESM2M. The global thermocline volumes (> 8°C) in ESM2M (173 $x10^{15}$ m^3) and ESM2G (131 $x10^{15}$ m^3) straddle the observations (145$x10^{15}$ m^3 for present day; 137 $x10^{15}$ m^3 after accounting for 0.5°C warming over the historical period; Levitus et al., 2005). ESM2M biases and root-mean-square errors in global ocean salinity profile (Figure 3B) are smaller than those found in ESM2G. Both models underestimate the shallow salinity maximum and redistribute salinity into the deep ocean through the creation of overly saline (Figure 4D) and overly warm (Figure 4C) North Atlantic Deep Water with approximately the correct density. In the Southern Ocean, the observed upper water column inversion of the halocline is poorly simulated in ESM2M and entirely absent in ESM2G (Figure 3F). These biases are common in the CMIP3 class of models (Randall et al. 2007 supplemental material).

Shortwave radiation

Some of the major model accomplishments and continued challenges in the development of these models can be seen in model representation of the shortwave radiation budget. One of the most robustly interpretable satellite measurements is the shortwave albedo from the perspective of the top of the atmosphere (the flux off the earth normalized to the flux the earth receives by the sun; Figure 4A) as it requires none of the complicating factors involved in atmospheric corrections. This lens reveals the excellent statistical comparison between the observational and modeled fields (r^2 = 0.93 in ESM2M; r^2 = 0.92 in ESM2G). Still the bias patterns in both ESM2M (Figure 4B) and ESM2G (Figure 4C) demonstrate large scale patterns of: 1) overly high albedos over the Rocky Mountains, 2) overly high albedos in the Bering Sea and Greenland Sea and Barents Sea associated with relatively large amounts of sea ice (perhaps appropriate given that the model is preindustrial), 3) overly low albedos in the Southern Ocean, particularly the Atlantic sector, 4) overly high albedo near the coasts of California, Peru, Chile, Angola, and Namibia, low albedo in the eastern tropical ocean basins associated with excessive low cloud, and 5) farther offshore from these coasts, overly low albedo in the eastern tropical ocean basins, associated with too little low cloud.

As an indication of the role of atmospheric cloud-driven differences from present day observations, we show the downward radiation impinging on the land and ocean surface in Figure 4D. The major biases (Figures 4E and F) include the Amazon and India having far too little cloud cover resulting in overly high shortwave radiation reaching the surface. Over the ocean, the eastern boundary current upwelling areas and the entire Southern Ocean receive too much

radiation. The north equatorial and western Pacific regions also receive too much radiation, and the south equatorial Pacific region too little associated with the difficulties in representing the Inter-Tropical Convergence Zone (ITCZ). The Southern Ocean shortwave bias results in a lack of sea ice and thus a low surface albedo (Figure 4, bottom row) with major implications for the representation of the seasonal cycle of mixed layer dynamics in these models. On the land, the primary surface albedo biases are: northward extension of the African tropical region, low albedo all along the boreal polar region, and high albedos associated with excessive Northern Hemisphere sea ice.

Surface climate

The surface ocean patterns of temperature (SST) are preserved well in both ESM2M and ESM2G (Figure 5 top row, r^2 of 0.99 and 0.98, respectively). The major differences relative to present day observations are: a general cooling consistent with their being forced by 1860 radiative conditions, a general hemispheric bias of cold north Subpolar Pacific and warm Southern Ocean, an equatorial cold Pacific bias, and eastern boundary condition warm biases. These problems are all similar to biases seen in GFDL's CM2.1 and other models of this class (Delworth et al., 2006.; Wittenberg et al., 2006; Randall et al. 2007 supplemental material; Richter et al., 2011) with the biases in ESM2G (Figure 5C) slightly larger in each case. Both models do a fairly good job at representing Sea Surface Salinity (SSS) structure (Figure 5D-F; r^2=0.80 for ESM2M and r^2=0.76 for ESM2G). SSS bias patterns are quite similar between the two models with ESM2G (Figure 5F) again manifesting larger biases than ESM2M (Figure 5E). Harrison et al. (submitted) show that these surface salt biases in the Western North Atlantic (Figure 5D-F), which are driven by low biases in Atlantic-draining land precipitation and related

weak Amazon outflow, in turn drive the deep Atlantic temperature and salinity biases (Figure 3C, 3D).

As an overall indicator of the models' abilities to capture large scale circulation, Sea Surface Height (SSH) structure is well preserved in both models (Figure 5G-I; r^2=0.96 for ESM2M; r^2=0.92 for ESM2G) with the major bias common to both models being a lower North Atlantic as a consequence of its salinification. ESM2M and ESM2G exhibit opposing biases in meridional SSH gradient and Antarctic Circumpolar Current with Drake Passage transports being low in ESM2G (108 Sv) and high in ESM2M (164 Sv) compared to observational estimates (140 ± 6 Sv; Ganachaud, 2003). This difference between the models is most strongly seen southeast of New Zealand, where the strength and path of the ACC meanders show opposite biases relative to observed SSH.

Overall, both models reproduce most of present day observed precipitation patterns (Figure 6A-C), particularly well in Africa and Oceana. However, they also suffer from a variety of biases including the common 'Double ITCZ' problem of too much precipitation in the central and eastern Pacific south of the equator (Lin, 2007) and the 'Dry Amazon' problem of too little precipitation in both the equatorial Atlantic and equatorial South America (Delworth et al. 2006). In addition, ESM2G has too little precipitation in the Central Equatorial Pacific. Precipitation in both models is low in mid-northern latitudes and high in mid southern latitudes in accordance with the inter-hemispheric SST bias (Figure 5A-C).

Various features of the precipitation biases are further highlighted when one considers precipitation variability (Figure 6D-F). While the models do not represent the magnitude of precipitation in the observations, both show strong precipitation variability in the Amazon as

they get heavy precipitation in boreal winter, but very little in boreal summer. While both models appear to represent the patterns of precipitation magnitude in the Indian Ocean, ESM2G has much better precipitation variability than ESM2M in this region. Conversely, while both models have a low bias in central and western Equatorial Pacific precipitation, the variability is too high in ESM2M and too low in ESM2G as a consequence of their differing El Nino Southern Oscillation (ENSO) statistics.

Statistics of ENSO variability in both models are shown via the NINO3 Index (SST in 150°W-90°W, 5°S-5°N) in Figure 7. Like their parent model CM2.1 (Wittenberg et al., 2006; Wittenberg, 2009), both models exhibit a broad spectrum of ENSO variability consistent with observations with amplitude and frequency modulation on multi-decadal time scales. Relative to observations however, ESM2M partitions too much variability into inter-annual modes relative to the seasonal cycle (period = 1 year) while ESM2G does not partition enough variability into inter-annual modes with most variability locked in the seasonal cycle. While previous work has suggested a dominant role for the atmospheric component (Guilyardi et al., 2004; Guilyardi et al. 2009), our results highlight the crucial role of ocean formulation on ENSO behavior. This difference is likely due to the difference in climatological mean state simulations of west Pacific SST (Figure 5A-C) and surface mixing. Relative to ESM2M, the stronger west Pacific SST gradient in ESM2G prevents convection over Indonesia from spreading eastward during El Nino thus weakening the coupling between SST (central Pacific warming) and the wind response (westerly wind anomalies). This westward shifted wind response in ESM2G also reduces the time for wind-curl induced ocean Rossby waves to impact the western boundary, thus shortening the time available for equatorial thermocline adjustment to these wind

anomalies (Kirtman, 1997; Wittenberg, 2002; Capotondi et al., 2006). This westward constriction also gives the El Nino events less time to grow, further weakening the El Nino and shortening its period. While the climatological Eastern Equatorial Pacific SST in ESM2G is not very much higher than in ESM2M (Figure 5B-C), the subsurface is much colder, allowing for ESM2G to tap into a stronger thermal contrast for the seasonal upwelling and stronger seasonal cycle of NINO3 SST in ESM2G.

Ocean meridional mass and heat transport structure

Both ESM2M and ESM2G match observations of NADW formation and circulation by generating warm, salty Atlantic mid-latitude water flowing northward near the surface that becomes much denser as it is cooled by the atmosphere in high northern latitudes, sinks to depth and flows southward through and out of the basin (Figure 8A-C). While ESM2M (35 Sv) and ESM2G (22 Sv) span the observational estimates for the Florida Strait transport (31±1 Sv; Ganachaud, 2003; Schott et al., 1988), ESM2G builds a robust Gulf Stream transport (51 Sv) comparable to that in ESM2M (49 Sv) by 27°N. The magnitude and pattern of the Atlantic meridional circulation that results in the models is very similar both to each other and to the observations of Talley et al. (2003). Comparison with zonal mean profiles at 24°N from Talley (2003) and Ganachaud and Wunch (2003) give excellent agreement for the depth scale of streamfunction attenuation with ESM2G, while the southward flow is relatively shallow in ESM2M (Figure 8D). By 30°S (Figure 8E), this distinction is largely removed. Antarctic Bottom Water also flows into the Atlantic and upwells to about 3 km depth before flowing southward back out of the basin. In the North Pacific at 24°N (Figure 8F), ESM2G has a stronger deep

circulation than ESM2M. Between the South Pacific and South Indian 32°S (Figure 8G-I), there is little agreement between either the two observational estimates or model estimates. Compared to observationally based estimates of the Indonesian Through-Flow of 8-17 Sv, ESM2M gives a value of the high end (16 Sv) while the ESM2G value is excessive (22 Sv). ESM2G has 16 Sv of Southern Ocean transport into the deep Pacific while ESM2M has only 6 Sv (Figure 8G). In the Southern Indian Ocean (Figure 8H), the models both have smaller deep flows than indicated in the observations. Taking the Indo-Pacific as a whole (Figure 8I), shows ESM2G behaving similarly to the stronger Talley (2003) estimate and ESM2M behaving similarly to the weaker Ganachaud (2003) estimate.

Given that both ESM2M and ESM2G match observations of the meridional overturning circulation quite well, it is not surprising that they also match observations of global ocean heat well. The global ocean heat transports from the two ESMs are much closer to each other than are the different observational estimates (Figure 9). In the northern hemisphere, the model transports lie within the observational estimates, though the initiation of northward transport near the equator is shifted southward in both models by approximately 5°. In the southern hemisphere, the models lie within the observational estimate of Ganachaud and Wunch (2003), but have less southward heat transport than the reanalyses of NCEP and ECMWF. We suspect these errors are related to long-standing problems in climate model simulation of the cloud distribution, height, and brightness in the Southern Ocean (e.g. Delworth et al. 2006).

Sea Ice

Both models agree fairly well with the observed minimum in sea ice extent in both hemispheres (Figure 10) even when one considers the expected sea ice changes between the modeled pre-industrial period and the present day satellite observational period (Winton et al, 2006). ESM2G is too extensive in Northern Hemisphere winter while ESM2M has a low bias of similar magnitude in Southern Hemisphere winter. Relative to observations, both models have larger ice extent in the Northern Hemisphere. This is consistent with the common climate model bias pattern of warm Southern Hemisphere and cold Northern Hemisphere subpolar regions as shown in Figure 5 (see Randall et al 2007, Figure 8.2) which was also present in CM2.1 (Delworth et al 2006). The larger influence of ocean formulation on winter ice cover is consistent with studies showing that ocean circulation strongly controls winter sea ice extent (e.g. Winton 2004).

Ocean mixed layer dynamics

One of the fundamental differences between ESM2M and ESM2G is their treatment of the ocean surface mixed layer. ESM2M uses the vertically resolved k-profile parameterization (Large et al., 1994) while ESM2G uses a bulk energetic parameterization after Kraus and Turner (1967). These two parameterizations result in explicit diffusivities in ESM2M that are about a factor of 3 higher than ESM2G in the upper 200 m, below which both models have extremely low explicit values in the thermocline. Another important distinction between the models is that ESM2M requires the upper three 10m levels to interact while the isopycnal-layer model ESM2G can represent mixed layers as shallow as 2 m. To compare the model formulations with observations, we show climatologies for monthly minimum and maximum MLD using the Levitus (1982) 0.125 density criterion in Figure 11. The comparison of minimum MLD highlights

the relatively shallow summer Southern Ocean mixed layer values in these models. Much of this bias is associated with the surface shortwave bias (Figure 4E, F) and warm SST bias (Figure 5B, C), with ESM2G suffering more so from these biases than ESM2M. In addition, one can see the relatively stronger zonal equatorial gradient in ESM2G compared to ESM2M. ESM2G's extremely shallow values in many areas (5-10 m near Peru) highlight the capacity for ESM2G to maintain average mixed layers much shallower than ESM2M.

Comparison of maximum MLD (Figure 11D-F) illustrates that both models mix deeply in the North Atlantic consistent with their robust NADW formation (Figure 8), but not deeply enough in the Southern Ocean. At 50°S, observed MLDs reach 717 m, while those in ESM2M reach only 653 m and in ESM2G only 559 m. In the western North Pacific, observed MLDs don't exceed 232 m, while those in ESM2M reach 422 m and in ESM2G only 358 m. Overall, ESM2G (r^2=0.39) correlates better with observations than ESM2M (r^2=0.24) for minimum MLD, while both correlate equally with maximum MLD (r^2=0.41).

We examine the different character of interior processes in these two models through the models' propensities to create and maintain mode waters – minimally stratified zones within the main thermocline that have distinct minima in the vertical density gradient (also referred to as a thermostad or pycnostad). Mode waters form through Ekman pumping in regions of deep water columns where they can be isolated from the surface and advectively exported equatorward into the main thermocline. This mechanism serves in complement with deep water formation to ventilate the ocean interior at intermediate depths (e.g. Talley et al. 2003), and has been shown to be a critical supplier of nutrients to the tropics through the thermocline (Sarmiento et al., 2004).

Maps of the depth gradient in potential density ($d\rho_0/dz$; kg m^{-3} km^{-1}) are shown in Figure 12 for 300 m, 600 m and a meridional section along 160°W for World Ocean Atlas 2009 (Figure 12A, D, G, respectively), ESM2M (Figure 12B, E, H, respectively) and ESM2G (Figure 12C, F, I, respectively). Here we define mode waters with a stratification cutoff of 0.6 kg m^{-3} km^{-1}. At 300 m, both models do a reasonable job at representing regional variability in stratification with ESM2G (Figure 12C; r^2=0.78; bias=0.35) having slightly higher covariance with the observations (Figure 12A) but larger bias than ESM2M (Figure 12B; r^2=0.74; bias=-0.06). ESM2M reproduces the observed areas of mode water in the Southern Ocean between 40°S-50°S while ESM2G has too little. By 600 m, the distinction seen between the two ocean models is largely erased as neither ESM2M (Figure 12D) nor ESM2G (Figure 12E) are capable of maintaining the low stratification (mode water) regions observed throughout the Southern Ocean near 40°S, though ESM2M shows faint traces of lower stratification in that region that boost the r^2 from only 0.435 in ESM2G to 0.605 in ESM2M. The scope of these differences is also highlighted in meridional sections along 160°W shown in Figure 12. While observations (Figure 12G) show a single, large volume of low stratification between the isopycnals of σ_θ = 27.2 and σ_θ = 26.7 down to 900m at 50°S, these areas are restricted to depths shallower than 400m in ESM2M and are not well pronounced in ESM2G. The volume of mode water in the Southern Ocean above σ_θ = 27.2 the observations ($19x10^{15}$ m^3) is reproduced partially in ESM2M ($14x10^{15}$ m^3) and only a small amount in ESM2G ($2x10^{15}$ m^3).

ESM2M builds an extensive pool of minimally-stratified mode water in the central North Pacific at 300 m that is not observed. This large volume of North Pacific mode water in ESM2M above σ_θ = 26.7 ($2x10^{15}$ m^3) has only a small expression in ESM2G (Figure 12I). In the North

Atlantic at 300m, both models express low stratification, though this is more prominent in ESM2M. The North Atlantic mode water volume above σ_θ = 27.6 in ESM2G (2.2×10^{15} m^3) is only slightly higher than observations (2.5×10^{15} m^3) while ESM2M (4.7×10^{15} m^3) is approximately double. The propensity of GFDL's MOM-based models to create unrealistically large volumes of mode water in the Northern Hemisphere was previously described by Gnanadesikan et al (2007b) in the context of potential vorticity.

Ocean ideal age distributions

While it has no direct observational equivalent, the ocean ideal age tracer (Thiele and Sarmiento, 1990) serves as a valuable indicator of ocean ventilation as an amalgam analog of chlorofluorocarbon, radiocarbon and other tracers. After 1100 years of integration, ESM2M and ESM2G have very similar basin-average ages in both the Atlantic (230 years for ESM2M; 224 years for ESM2G) and Pacific (600 years for ESM2M, 650 years for ESM2G). The vertical age structure, however, strongly differs between the two models with ESM2G having a much older upper water column but younger deep waters than ESM2M. The deep patterns are a direct consequence of the differences in the models' meridional overturning (Figure 8). In the North Atlantic, relatively old bottom water persists in ESM2M while ESM2G ventilates to the bottom. Similarly in the Pacific, the larger supply of Indo-Pacific bottom waters in ESM2G makes it much younger than ESM2M.

Much of the upper water column age difference between these two models can be tracked to the shallower thermocline in ESM2G than ESM2M (Figure 13, bottom row). Even though the thermocline volume (> 8°C) is much larger in ESM2M than in ESM2G, their average

age is similar (86 years in ESM2G; 81 years in ESM2M). While the causality behind this different behavior is not completely understood, we suspect that it is related to the propensity of ESM2G to maintain coherence in water mass properties compared to ESM2M. As was noted above, explicit levels of vertical diffusion in these two models are much higher in ESM2M than in ESM2G both within and just below the mixed layer. In the tropical thermocline, ESM2M diffusivities are generally lower than ESM2G diffusivities. Further analysis and sensitivity studies are required to disentangle the relative controls determining these important differences.

A combined view of Southern Ocean zonal mean age (color), meridional density (σ_θ; black lines) and zonally-integrated meridional overturning (green) in ESM2M (Figure 14A) and ESM2G (Figure 14B) highlights how differently these two models respond under conditional stability in deeply convective areas. Contours of density illustrate ESM2M's stronger meridionally sloping isopycnals between 45°S and 60°S consistent with the deeper maximum mixed layer depths in ESM2M than ESM2G (Figure 11). Stream function contours illustrate the far deeper southward flow in ESM2M resulting in a much young upper water column (color) than in ESM2G. South of the deep mixing region, westerly winds drive perpetual Ekman upwelling supplying relatively dense waters that maintain an upper water column density gradient to prevent deep wintertime convection. The transport of those dense waters to the north supports deep wintertime convection with associated intense heat loss. This dynamic operates similarly in these models with both having maximum northward transports of approximately 25 Sv and deep wintertime convection. Because the meridional temperature gradient is strongest in the deep convective region and decreases to the north, horizontal

mixing in the meridional direction provides a significant local cooling. In ESM2M, this effect is strong enough to overcome the weak vertical stratification in the deep wintertime convection region to invert the vertical density gradient and induce further convection. Because horizontally adjacent layers only interact within the mixed layer in ESM2G, and isopycnal mixing does not induce significant cooling, convection occurs only in the mixed layer during wintertime with southward flow restricted to a fairly shallow depth (Figure 14B).

In ESM2M, at least three mechanisms drive enhanced lateral mixing, and subsequent enhanced convection and deepening southward circulation of the Deacon Cell relative to ESM2G. First, lateral mixing that is otherwise oriented along locally-referenced potential density surfaces defaults to horizontal, diapycnal mixing when slopes increase beyond the threshold of 1/200. Second, the vertical transition between the surface-oriented sub-mesoscale scheme (Fox-Kemper et al., 2011) and deeper-scale thickness mixing parameterization (Gent and McWilliams, 1990) drives a secondary subsurface overturning circulation stimulating convection. Finally, high shear at the edge of the Antarctic Circumpolar Current induces significant exchange across the meridional temperature gradient. Given these complex interactions, we suggest that further development of parameterizations relating to convection is warranted. Potential development foci include improved representation of mechanisms such as eddies (e.g. Boning et al., 2008), storms, and propagating waves. Attribution and correction of ocean biases in the Southern Ocean would also benefit from amelioration of the atmospheric biases in radiative transfer (Figure 4) that drive overly warm SST biases (Figure 5) and enhanced summer surface stratification in these models.

Conclusions

In summary, we have developed two new Earth System Models (ESM2M and ESM2G) that differ only in ocean formulation. This work is unique in exploring an isopycnal coordinate ocean compared to the more traditional pressure coordinate regarding a suite of factors influencing climate. Climate simulation quality was found to be generally very similar to GFDL's earlier CM2.1. Both ESM2M and ESM2G have realistic net radiative patterns at the top of the atmosphere and heat transports in the atmosphere and ocean. Problems the two models share are weak rainfall in the Amazon region, and the Southern Ocean surface being both too warm and mixing being too shallow. Demonstrating the importance of ocean configuration on climate fidelity, the two models straddle observed estimates for a number of climate indices including: ENSO variability being overly strong in ESM2M and weak in ESM2G, the volume of the thermocline being too deep in ESM2M and slightly too shallow in ESM2G, deep Pacific ventilation being relatively weak in ESM2M (6 Sv) and strong in ESM2G (16 Sv), and North Pacific thermocline ventilation being too strong in ESM2M. While each model has its relative strengths and weaknesses, our overall assessment of the models is that their quasi-equilibrium simulations both achieve sufficient fidelity to allow meaningful perturbation studies. In the companion paper (Part II), we describe the implications of these differences for simulation of the preindustrial carbon cycle. In future papers, we will apply these models to evaluate the impact of human activities on past and future climate changes.

Acknowledgements

Tony Rosati, Anand Gnanadesikan, Jorge Sarmiento, Joellen Russell, Robbie Toggweiler and Stephanie Downes provided valuable insights on Southern Ocean circulation that assisted in our interpretation.

References

Adcroft, A., R. W. Hallberg, and M. J. Harrison, 2008: A finite volume discretization of the pressure gradient force using analytic integration. *Ocean Modelling*, **22**, doi:10.1016/j.ocemod.2008.02.001.

Adcroft, A., J. R. Scott, and J. Marotzke (2001), Impact of geothermal heating on the global ocean circulation, *Geophys. Res. Lett.*, **28**, 1735–1738, doi:10.1029/2000GL012182.

Adcroft, A. and J.-M. Campin, 2004: Rescaled height coordinates for accurate representation of free-surface flows in ocean circulation models. *Ocean Modelling*, **7**, 269–284.

Anderson, J. L., V. Balaji, A. J. Broccoli, W. F. Cooke, T. L. Delworth, K. W. Dixon, L. J. Donner, K. A. Dunne, S. Freidenreich, S. T. Garner, R. Gudgel, C. T. Gordon, I. Held, R. S. Hemler, L. Horowitz, S. A. Klein, T. R. Knutson, P. J. Kushner, A. R. Langenhorst, N.-C. Lau, Z. Liang, S. Malyshev, P. C. D. Milly, M. J. Nath, J. J. Ploshay, V. Ramaswamy, M. D. Schwarzkopf, E. Shevliakova, J. J. Sirutis, B. J. Soden, W. F. Stern, L. T. Sentman, R. J. Wilson, A. T. Wittenberg, and B. Wyman, 2004: The New GFDL global atmosphere and land model AM2–LM2: Evaluation with prescribed SST simulations. *J. Climate*, **17**, 4641-4673.

Antonov, J. I., R. A. Locarnini, T. P. Boyer, A. V. Mishonov, and H. E. Garcia, 2006. World Ocean Atlas 2005, Volume 2: Salinity. S. Levitus, Ed. NOAA Atlas NESDIS 62, U.S. Government Printing Office, Washington, D.C., 182 pp.

Antonov, J. I., D. Seidov, T. P. Boyer, R. A. Locarnini, A. V. Mishonov, H. E. Garcia, O. K. Baranova, M. M. Zweng, and D. R. Johnson, 2010. World Ocean Atlas 2009, Volume 2: Salinity. S. Levitus, Ed. NOAA Atlas NESDIS 69, U.S. Government Printing Office, Washington, D.C., 184 pp.

Boning , C. W., A. Dispert, M. Visbeck, S. R. Rintoul, and F. U. Schwarzkopf, 2008: The response of the Antarctic Circumpolar Current to recent climate change. *Nature Geosci.*, **1**, 864–869.

Bryan, K. and L. J. Lewis, 1979: A water mass model of the world ocean. *J. Geophys. Res.*, **84**, 2503–2517.

Capotondi, A., A. Wittenberg, and S. Masina, 2006: Spatial and temporal structure of tropical Pacific interannual variability in 20th century coupled simulations. *Ocean Modelling*, **15**, 274-298.

Danabasoglu, G., W. G. Large, J. J. Tribbia, P. R. Gent, B. P. Briegleb, and J. C. McWilliams, 2006: Diurnal coupling in the tropical oceans of CCSM3. *J. Climate.*, **19**, 2347–2365.

Danabasoglu, G. and J. C. McWilliams, 1995: Sensitivity of the global ocean circulation to parameterizations of mesoscale tracer transports. *J. Climate*, **8**, 2967–2987.

Delworth, T. D., S. Manabe, and R. J. Stouffer, 1993: Interdecadal variations of the thermohaline circulation in a coupled ocean-atmosphere model, *J. Clim*ate, **6**, 1993:2011.

Delworth, T.D., A.J. Broccoli, A. Rosati, R.J. Stouffer, V. Balaji, J.A. Beesley, W.F. Cooke, K.W. Dixon, J. Dunne, K.A. Dunne, J.W. Durachta, K.L.Findell, P. Ginoux, A. Gnanadesikan, C.T. Gordon, S.M. Griffies, R. Gudgel, M.J. Harrison, I.M. Held, R.S. Hemler, L.W. Horowitz, S.A. Klein, T.R. Knutson, P.J. Kushner, A.R. Langenhorst, H.-C. Lee, S.-J. Lin, J. Lu, S.L. Malyshev, V. Ramaswamy, J. Russell, M.D. Schwarzkopf, E. Shevliakova, J.J. Sirutis, M.J. Spelman, W.F. Stern, M. Winton, A.T. Wittenberg, B. Wyman, F. Zeng, and R. Zhang, 2006: GFDL's CM2 global coupled climate models-Part I: Formulation and simulation characteristics. *J. Climate*, **19**, 643-674.

Donner, L. J., B. Wyman, R. S. Hemler, L. Horowitz, Y. Ming, M. Zhao, J-C Golaz, P. Ginoux, S.-J. Lin, M. D. Schwarzkopf, J. Austin, G. Alaka, W. F. Cooke, T. L. Delworth, S. Freidenreich, C. T.

Gordon, S. Griffies, I. Held, W. J. Hurlin, S. A. Klein, T. R. Knutson, A. R. Langenhorst, H. C. Lee, Y. Lin, B. I. Magi, S. Malyshev, V. Naik, M. J. Nath, R. Pincus, J. J. Ploshay, V. Ramaswamy, C. J. Seman, E. Shevliakova, J. J. Sirutis, W. F. Stern, R. J. Stouffer, R. J. Wilson, M. Winton, A. T. Wittenberg, and F. Zeng, 2011: The dynamical core, physical parameterizations, and basic simulation characteristics of the atmospheric component AM3 of the GFDL Global Coupled Model CM3. *J. Climate*, **24**, doi:10.1175/2011JCLI3955.1.

Downes, S. M., A. Gnanadesikan, S. M. Griffies, and J. L. Sarmiento, 2011: Water mass exchange in the Southern Ocean in coupled climate models. J*. Phys. Oceano*., doi:10.1175/2011JPO4586.1. 4/11.

Dunne, J. P., R. A. Armstrong, A. Gnanadesikan, J. L. Sarmiento, and R. D. Slater, 2005: Empirical and mechanistic models for particle export ratio. *Global Biogeochem. Cycles*, **18**, doi:10.1029/2004GB002390.

Dunne, J. P., J. L. Sarmiento, and A. Gnanadesikan, 2007: A synthesis of global particle export from the surface ocean and cycling through the ocean interior and on the seafloor, *Global Biogeochem. Cycles*, **21**, doi:10.1029/2006GB002907.

Dunne, J. P., A. Gnanadesikan, J. L. Sarmiento and R. D. Slater, 2010 Technical description of the prototype version (v0) of Tracers of Phytoplankton with Allometric Zooplankton (TOPAZ) ocean biogeochemical model as used in the Princeton IFMIP model, Biogeosciences Supplement, 7, 3593.

Easter, R. C., 1993: Two modified versions of Bott's positive-definite numerical advection scheme. Mon. Wea. Rev., **121**, 297–304.

Farneti, R., T. Delworth, A. Rosati, S. Griffies, and F. Zeng, 2010: The role of mesoscale eddies in the rectification of the Southern Ocean response to climate change. *J. Phys. Oceanogr.*, **40**, 1539– 1557.

Ferrari, R., S. Griffies, A. Nurser, and G. Vallis, 2010: A boundary-value problem for the parameterized mesoscale eddy transport. *Ocean Modelling*, **32**, 143–156.

Fetterer, F., K. Knowles, W. Meier, and M. Savoie. 2002, updated 2009. Sea Ice Index. Boulder, CO: National Snow and Ice Data Center. Digital media.

Fox-Kemper, B., G. Danabasoglu, R. Ferrari, S. M. Griffies, R. W. Hallberg, M. Holland, S. Peacock, and B. Samuels, 2011: Parameterization of mixed layer eddies. III: Global implementation and impact on ocean climate simulations. *Ocean Modelling*, doi:10.1016/j.ocemod.2010.09.002.

Fox-Kemper, B., R. Ferrari, and R. Hallberg, 2008: Parameterization of mixed layer eddies. I: Theory and diagnosis. *J. Phys. Oceanogr.*, **38**, 1145–1165.

Friedrichs, M A., J A Dusenberry, L A Anderson, R A Armstrong, F Chai, J R Christian, S C Doney, John P Dunne, M Fujii, R Hood, D J McGillicuddy, Jr, J K Moore, M Schartau, Y H Spitz, and J D Wiggert, 2007: Assessment of skill and portability in regional marine biogeochemical models: Role of multiple planktonic groups. *J. Geophys. Res.*, **112**, C08001, doi:10.1029/2006JC003852.

Horowitz, L.W., S. Walters, D.L. Mauzerall, L.K. Emmons, P.J. Rasch, C. Granier, X.X. Tie, J.-F. Lamarque, M.G. Schultz, G.S. Tyndall, J.J. Orlando, and G.P. Brasseur, A global simulation of tropospheric ozone and related tracers: Description and evaluation of MOZART, version 2, *J. Geophys. Res.*, **108**(D24), 4784, doi:10.1029/2002JD002853, 2003.,

Ganachaud, A., and C. Wunsch, 2003: Large-scale ocean heat and freshwater transports during the World Ocean Circulation Experiment. *J. Climate*, **16**, 696-705.

Garcia, H. E., R. A. Locarnini, T. P. Boyer, J. I. Antonov, O. K. Baranova, M. M. Zweng, and D. R. Johnson, 2010a. World Ocean Atlas 2009, Volume 3: Dissolved Oxygen, Apparent Oxygen Utilization, and Oxygen Saturation. S. Levitus, Ed. NOAA Atlas NESDIS 70, U.S. Government Printing Office, Washington, D.C., 344 pp.

Garcia, H. E., R. A. Locarnini, T. P. Boyer, J. I. Antonov, M. M. Zweng, O. K. Baranova, and D. R. Johnson, 2010b. World Ocean Atlas 2009, Volume 4: Nutrients (phosphate, nitrate, silicate). S. Levitus, Ed. NOAA Atlas NESDIS 71, U.S. Government Printing Office, Washington, D.C., 398 pp.

Gargett, A. E. and G. Holloway, 1984: Dissipation and diffusion by internal wave breaking. *J. Mar. Res.*, **42**, 15-27.

Gent, P. R. and J. C. McWilliams, 1990: Isopycnal mixing in ocean circulation models. *J. Phys. Oceanogr.*, **20**, 150–155.

Gent, P. R., J.Willebrand, T. J. McDougall, and J. C. McWilliams, 1995: Parameterizing eddy-induced tracer transports in ocean circulation models. Journal of Physical Oceanography, **25**, 463–474.

Gibson, J.K., P. Kallberg, S. Uppala, A. Hernandez, A. Nomura, and E. Serrano, 1997: ERA Description. Vol 1. ECMWF Re-analysis Project Rep. Series, European Centre for Medium-Range Weather Forecasts, Reading, United Kingdom, 66 pp.

Gnanadesikan, A., S. Griffies, and B. Samuels, 2007a: Effects in a climate model of slope tapering in neutral physics schemes. *Ocean Modelling*, **17**, 1–16.

Gnanadesikan, A., J L Russell, and F. Zeng, 2007b: How does ocean ventilation change under global warming? *Ocean Science*, **3**, 43-53.

Gnanadesikan, A. et al., 2006: GFDL's CM2 global coupled climate models-Part 2: The baseline ocean simulation. *J. Climate*, **19**, 675–697.

Griffies, S. M., 1998: The Gent-McWilliams skew-flux. *J. Phys. Oceanogr.*, **28**, 831–841.

Griffies, S. M., 2004: Fundamentals of Ocean Climate Models. Princeton University Press, Princeton, USA, 518+xxxiv pages.

Griffies, S. M., 2009: Elements of MOM4p1: GFDL Ocean Group Technical Report No. 6. NOAA/Geophysical Fluid Dynamics Laboratory, Princeton, USA, 444 pp.

Griffies, S. M., A. Gnanadesikan, R. C. Pacanowski, V. Larichev, J. K. Dukowicz, and R. D. Smith, 1998: Isoneutral diffusion in a z-coordinate ocean model. *J. Phys. Oceanogr.*, **28**, 805–830.

Griffies, S. M., et al., 2005: Formulation of an ocean model for global climate simulations. Ocean Science, 1, 45–79.

Griffies, S., and R. W. Hallberg, 2000: Biharmonic friction with a Smagorinsky-like viscosity for use in large-scale eddy-permitting ocean models. *Monthly Weather Review*, **128**, 2935-2946.

Guilyardi, E., S. Gualdi, J. Slingo, A. Navarra, P. Delecluse, J. Cole, G. Madec, M. Roberts, M. Latif, and L. Terray, 2004: Representing El Nino in coupled ocean-atmosphere GCMs: The dominant role of the atmospheric component. *J. Climate*, **17**, 4623-4629.

Guilyardi, E., A. Wittenberg, A. Fedorov, M. Collins, C. Wang, A. Capotondi, G. J. van Oldenborgh, and T. Stockdale, 2009: Understanding El Niño in ocean-atmosphere general circulation models: Progress and challenges. *Bull. Amer. Meteor. Soc.*, **90**, 325-340. doi:10.1175/2008BAMS2387.1

Hallberg, R., 1995: Some aspects of the circulation in ocean basins with isopycnals intersecting the sloping boundaries. Ph.D. thesis, University of Washington, 244 pp. [Available from University Microfilms, 1490 Eisenhower Place, P.O. Box 975, Ann Arbor, MI 48106.]

Hallberg, R. W., 1997: Stable split time stepping schemes for large-scale ocean modeling. *J. Comp. Phys.*, **135**, 54-65.

Hallberg, R. W., 2000: Time integration of diapycnal diffusion and Richardson number-dependent mixing in isopycnal coordinate ocean models. *Mon. Weather Rev.*, **128**, 1402-1419.

Hallberg, R., 2003: The suitability of large-scale ocean models for adapting parameterizations of boundary mixing and a description of a refined bulk mixed layer model. *Near-Boundary Processes and Their Parameterization: Proc. ʻAha Hulikoʻa Hawaiian Winter Workshop,* Honolulu, HI, University of Hawaii at Manoa, 187–203.

Hallberg, R., 2005: A thermobaric instability of Lagrangian vertical coordinate ocean models. *Ocean Modelling*, **8**, doi:10.1016/j.ocemod.2004.01.001.

Hallberg, R., and A. Adcroft, 2009: Reconciling estimates of the free surface height in Lagrangian vertical coordinate ocean models with mod-split time stepping. *Ocean Modelling*, **29**, 15-26.

Harrison, M. J., and R. W. Hallberg, 2008: Pacific subtropical cell response to reduced equatorial dissipation. *J. Phys. Oceanogr.*, **38**, 1894-1912.

Harrison, M., R. Hallberg, and A. J. Adcroft, submitted on 6/28/2011: Impact of large-scale tropical precipitation anomalies on the overturning and interior watermass structure of a coupled climate model. J Clim.Henson, S. A., J. P. Dunne, and J. L. Sarmiento, 2009: Decadal variability in North Atlantic phytoplankton blooms. *J. Geophys. Res.*, **114**, C04013, doi:10.1029/2008JC005139.

Henson, S. A., J. L Sarmiento, J. P. Dunne, L. Bopp, I. Lima, S. C. Doney, J. John, and C. Beaulieu, February 2010: Detection of anthropogenic climate change in satellite records of ocean chlorophyll and productivity. *Biogeosciences*, **7**, 621-640.

Henyey, F. S., J. Wright, and S. M. Flatté, 1986: Energy and action flow through the internal wave field: An eikonal approach. *J.Geophys. Res.,* **91,** 8487–8496.

Kalnay, E., and Co-authors, 1996: The NCEP/NCAR 40-year re-analysis project. *Bull. Amer. Meteor. Soc.*, **77**, 437-471.

Key, R. M., Kozyr, A., Sabine, C. L., Lee, K., Wanninkhof, R., Bullister, J., Feely, R. A., Millero, F., Mordy, C., and Peng, T.-H., 2004: A global ocean carbon climatology: results from GLODAP, *Glob. Biogeochem.Cycles.*, **18**, GB4031, doi:10.1029/2004GB002247.

Kirtman, B. P., 1997: Oceanic Rossby wave dynamics and the ENSO period in a coupled model. *J. Climate*, **10**, 1690-1704.

Klaas, C., and D. Archer (2002), Association of sinking organic matter with various types of mineral ballast in the deep sea: Implications for the rain ratio, *Glob. Biogeochem. Cycles*, **16**, 1116, doi:10.1029/2001GB001765.

Klausmeier, C.A., E. Litchman, T. Daufresne and S.A. Levin. 2004. Optimal N:P stoichiometry of phytoplankton. *Nature*, **429**, 171-174.

Kraus, E.B., and Turner, J.S. (1967) A One Dimensional Model of the Seasonal Thermocline. II The General Theory and its Consequences. *Tellus*, **19**, 98-106.

Large, W., and S. Yeager, 2004: Diurnal to decadal global forcing for ocean and sea-ice models: the data sets and flux climatologies. NCAR Technical Note: NCAR/TN-460+STR. CGD Division of the National Center for Atmospheric Research.

Large, W. G., G. Danabasoglu, S. C. Doney, and J. C. McWilliams, 1997: Sensitivity to surface forcing and boundary layer mixing in a global ocean model: annual-mean climatology. *J. Phys. Oceanogr.*, **27**, 2418–2447.

Large, W. G., G. Danabasoglu, J. C. McWilliams, P. R. Gent, and F. O. Bryan, 2001: Equatorial circulation of a global ocean climate model with anisotropic horizontal viscosity. *J. Phys. Oceanogr.*, **31**, 518–536.

Large,W. G., J. C. McWilliams, and S. C. Doney, 1994: Oceanic vertical mixing: A review and a model with a nonlocal boundary layer parameterization. *Rev. Geophys.*, **32**, 363–403.

Lee, H.-C., A. Rosati, and M. Spelman, 2006: Barotropic tidal mixing effects in a coupled climate model: Oceanic conditions in the northern Atlantic. *Ocean Modelling*, **3-4**, 464–477.

Legg, S., R. W. Hallberg, and J B Girton, 2006: Comparison of entrainment in overflows simulated by z-coordinate, isopycnal and non-hydrostatic models. *Ocean Modelling*, **11**, doi:10.1016/j.ocemod.2004.11.006.

Levitus, S. 1982, Climatological Atlas of the World Ocean, NOAA Professional Paper 13, U.S. Department of Commerce.

Levitus, S, J. Antonov, and T. Boyer, 2005: Warming of the world ocean, 1955–2003. *Geophys. Res. Lett.*, VOL. 32, L02604, doi:10.1029/2004GL021592

Lin, JL 2007: The Double-ITCZ Problem in IPCC AR4 Coupled GCMs: Ocean–Atmosphere Feedback Analysis, *J. Climate*, **20**, 4497–4525.

Locarnini, R. A., A. V. Mishonov, J. I. Antonov, T. P. Boyer, and H. E. Garcia, 2006. World Ocean Atlas 2005, Volume 1: Temperature. S. Levitus, Ed. NOAA Atlas NESDIS 61, U.S. Government Printing Office, Washington, D.C., 182 pp.

Locarnini, R. A., A. V. Mishonov, J. I. Antonov, T. P. Boyer, H. E. Garcia, O. K. Baranova, M. M. Zweng, and D. R. Johnson, 2010. World Ocean Atlas 2009, Volume 1: Temperature. S. Levitus, Ed. NOAA Atlas NESDIS 68, U.S. Government Printing Office, Washington, D.C., 184 pp.

Marshall, J., C. Hill, L. Perelman, and A. Adcroft, 1997: Hydrostatic, quasi-hydrostatic, and non-hydrostatic ocean modeling. *J. Geophys. Res.*, **102**, 5733–5752.

Martin, T, and A. Adcroft, 2010: Parameterizing the fresh-water flux from land ice to ocean with interactive icebergs in a coupled climate model. *Ocean Modelling*, **34**, doi:10.1016/j.ocemod.2010.05.001.

Milly, P.C.D. et al. in preparation: Enhanced representation of land physics for earth-system modeling. J. *Hydroclimatology*.

Murray, R.J., 1996: Explicit generation of orthogonal grids for ocean models. Journal of Computational Physics, vol. 126, pages 251-273.

Najjar, R., and J. C. Orr (1998), Design of OCMIP-2 simulations of chlorofluorocarbons, the solubility pump and common biogeochemistry, internal OCMIP report, 25 pp., LSCE/CEA Saclay, Gif-sur-Yvette, France.

Olson, J. S., J. A. Watts, L. J. Allison, 1985: Major world ecosystem complexes ranked by carbon in live vegetation: a database. Carbon Dioxide Infromation Center numerical Data Collection, NDP-017, Oak Ridge, TN, DOI:10.3334/CDIAC/lue.ndp017.

Perovich, D., T.C. Greenfell, B., Light, and P.V. Hobb, 2002: Seasonal evolution of the albedo of multiyear Arctic sea ice. Journal of Geophysical Research, 107, 8044, doi:10.1029/2000JC000438.

Polovina, J J., J. P. Dunne, P. A. Woodworth, and E. A. Howell, 2011: Projected expansion of the subtropical biome and contraction of the temperate and equatorial upwelling biomes in the North Pacific under global warming. *ICES Journal of Marine Science*, doi:10.1093/icesjms/fsq198. 2/11.

Randall, D.A., R.A. Wood, S. Bony, R. Colman, T. Fichefet, J. Fyfe, V. Kattsov, A. Pitman, J. Shukla, J. Srinivasan, R.J. Stouffer, A. Sumi and K.E. Taylor, 2007: Climate Models and Their Evaluation. In: Climate Change 2007: The Physical Science Basis. Contribution of Working Group I to the Fourth Assessment Report of the Intergovernmental Panel on Climate Change [Solomon, S., D. Qin, M. Manning, Z. Chen, M. Marquis, K.B. Averyt, M.Tignor and H.L. Miller (eds.)]. Cambridge University Press, Cambridge, United Kingdom and New York, NY, USA.

Richter, I., S.-P. Xie, A. T. Wittenberg, and Y. Masumoto, 2011: Tropical Atlantic biases and their relation to surface wind stress and terrestrial precipitation. *Climate Dyn.*, doi: 10.1007/s00382-011-1038-9.

Saba, V. S., and J. P. Dunne, et al., 2010: Challenges of modeling depth-integrated marine primary productivity over multiple decades: A case study at BATS and HOT. *Glob. Biogeochem. Cycles*, **24**, GB3020, doi:10.1029/2009GB003655.

Sarmiento, J. L., R. D. Slater, J. P. Dunne, A. Gnanadesikan, and M. R. Hiscock, November 2010: Efficiency of small scale carbon mitigation by patch iron fertilization. *Biogeosciences*, **7**, 3593-3624.

Schott, F. A., T. N. Lee, and R. Zantopp, Variability of structure and transport of the Florida Current in the period range of day to seasonal, *J. Phys. Oceanogr.*, **18**, 1209– 1230, 1988.

Shevliakova, E., S. W. Pacala, S. Malyshev, P. C. D. Milly, and L. T Sentman, et al., 2009: Carbon cycling under 300 years of land use change: Importance of the secondary vegetation sink. *Glob. Biogeochem.Cycles*, **23**, GB2022, doi:10.1029/2007GB003176.

Simmons, H. L., S. R. Jayne, L. C. St. Laurent, and A. J. Weaver, 2004: Tidally driven mixing in a numerical model of the ocean general circulation. *Ocean Modelling*, **6**, 245–263.

Smagorinsky, J., 1993: Some historical remarks on the use of non-linear viscosities - 1.1 Introductory remarks In Large Eddy Simulation of Complex Engineering and Geophysical Flows, Proceedings of an International Workshop in Large Eddy Simulation, Cambridge, UK, Cambridge University Press, 1-34.

Smith, T.M., R. W. Reynolds, T. C. Peterson, and J. Lawrimore, 2008: Improvements to NOAA's historical merged land-ocean surface temperature analysis (1880-2006). *J. Climate*, **21**, 2283-2296.

Stacey, M.W., S. Pond, and Z. P. Nowak, 1995: A numerical model of the circulation in Knight Inlet, British Columbia, Canada. *J. Phys. Oceanogr.*, **25**, 1037–1062.

Stouffer, R. J., A. J. Weaver, and M. Eby, 2004: A method for obtaining pre-twentieth century initial conditions for use in climate change studies. *Climate Dynamics*, **23**, 327-339.

Takahashi T., S. C. Sutherland, R. Wanninkhof, C. Sweeney, R. A. Feely, D. W. Chipman, B. Hales, G. Friederich, F. Chavez, C. Sabine, A. Watson, D. C.E. Bakker, U. Schuster, N. Metzl, H. Yoshikawa-Inoue, M. Ishii, T. Midorikawa, Y. Nojiri, A. Körtzinger, T. Steinhoff, M. Hoppema, J. Olafsson, T. S. Arnarson, B. Tilbrook, T. Johannessen, A. Olsen, R. Bellerby, C.S. Wong, B. Delille, N.R. Bates, and H. J.W. de Baar :2009 Climatological mean and decadal change in surface ocean pCO_2, and net sea–air CO_2 flux over the global oceans. *Deep-Sea Res. II*, **56**, 554-577.

Talley, L. D., 2003: Shallow, intermediate and deep overturning components of the global heat budget. *J. Phys. Oceanogr.*, **33**, 530–560.

Talley, L. D., J.L Reid, P. E. Robbins, 2003: Data-based meridional overturning streamfunctions for the global ocean. *J. Climate*, **16**, 3213-3226.

Thiele, G., and J. L. Sarmiento, 1990: Tracer Dating and Ocean Ventilation. J. Geophys. Res., 95, 9377-9391.

Thompson, L. K. A. Kelly, D. Darr and R. Hallberg, 2003. Buoyancy and mixed-layer effects on the Sea Surface Height Response in an isopycnal model of the North Pacific. *J. Phys. Oceanogr.*, **32**, 3657–3670.

Winton, M. 2003: On the climatic impact of ocean circulation. *J. Climate*, **16**, 2875-2889.

Wittenberg, A. T., 2002: ENSO response to altered climates. Ph. D. Thesis, Princeton University, 462pp.

Wittenberg, A. T., 2009: Are historical records sufficient to constrain ENSO simulations? *Geophys. Res. Lett.*, **36**, L12702. doi:10.1029/2009GL038710.

Wittenberg, A. T., A. Rosati, N.-C. Lau, and J. J. Ploshay, 2006: GFDL's CM2 global coupled climate models. Part III: Tropical Pacific climate and ENSO. *J. Climate*, **19**, 698-722.

Figures:

Figure 1: Box diagram of an earth system model. The green shaded boxes highlight the components needed to close the carbon cycle in a climate model (the blue and yellow shaded boxes). Note that the atmospheric chemistry and aerosol distributions in the versions described here are externally specified.

Figure 2: Globally averaged time series of various physical climate quantities over the first 1000 years of integration for ESM2M (red) and ESM2G (green): A) Net radiation at the top of the model atmosphere in W m^{-2} with positive values indicating a warming of the atmosphere; B) Surface (2m) air temperature in °C; C) Net heat flux into the ocean – sea ice system in units of W m^{-2}. Positive values indicate a warming of the ocean; D) Sea surface temperature (SST) in units of °C; E) Volume average ocean temperature in units of °C; F) Atlantic Meridional Overturning Circulation (AMOC) calculated from the maximum value for the Atlantic meridional overturning streamfunction over all depths and latitudes between 20°N and 60°N.

Figure 3: Depth profiles of temperature (left panels) and salinity (right panels). The top panels are global averages. The middle panels are averages taken from the Atlantic Ocean, bottom panels from the Southern Ocean for observations (World Ocean Atlas 2009; black),. ESM2M (red), and ESM2G (green).

Figure 4: Observationally derived present day estimates (A, D, G) and preindustrial difference/bias patterns in ESM2M (B, E, H) and ESM2G (C, F, I) for shortwave radiation albedo at the top of the atmosphere (A-C), downward shortwave radiation onto the surface land/ocean (D-F) and surface shortwave albedo (G-I). Observations are averages for the period of 1984-2007 based on NASA LaRC/GEWEX Surface Radiation Budget project Release 3.0

(http://eosweb.larc.nasa.gov/PRODOCS/srb/table_srb.html). These data were obtained from the NASA Langley Research Center Atmospheric Science Data Center. Model values are averages from years 501-600 of model integration.

Figure 5: Sea surface temperature (SST; top row; °C), Sea surface salinity (SSS; middle row; PSU) and sea surface height (SSH; bottom row; m). In each case, the left column is an observational estimate while middle (ESM2M) and right (ESM2G) columns are the model anomalies (model minus observations). SST (Locarnini et al. 2010) and SSS observations (Antonov et al. 2010) are from the World Ocean Altas 2009 (http://www.nodc.noaa.gov/OC5/WOA09/pr_woa09.html) while SSH observations are from Maximenko and Niiler (2005; http://apdrc.soest.hawaii.edu/projects/DOT/). On the model anomaly maps are plotted the bias, correlation coefficient and standard error between the model and observationally based fields. Note that some of these biases (most notably temperature) are expected in comparison of preindustrial models states with present day observations.

Figure 6: Precipitation climatology (top row; m a^{-1}) and standard deviation of monthly means (bottom row; m a^{-}). In each case, the left column is an observational estimate from Mirador TRMM version 3B43 from 1998-2010 (http://mirador.gsfc.nasa.gov/collections/TRMM_3B43__006.shtml) . The data used in this effort were acquired as part of the activities of NASA's Science Mission Directorate, and are archived and distributed by the Goddard Earth Sciences (GES) Data and Information Services Center (DISC). The middle (ESM2M) and right (ESM2G) columns are the corresponding model derived fields based on years 301-500.

Figure 7: NINO3 (150°W-90°W; 5°S-5°N) SST power spectra (°C octave^{-1}) versus period (year) from NOAA's extended reconstruction version 3 for 1880-2010 (Smith et al., 2008; http://www.ncdc.noaa.gov/oa/climate/research/sst/ersstv3.php), and years 301-500 for ESM2M (red and ESM2G (green).

Figure 8: Top row: Latitude versus depth plot of the overturning stream-function in the Atlantic Basin. The observational estimates (left panel) are from Talley et al. 2003. The middle panel is from ESM2M, right from ESM2G. Middle and bottom rows: Depth distributions of the over turning stream-function at various zonal bands for the different ocean basins. ESM2M data is represented by the red lines, ESM2G by the green lines. The open circles are from Talley (2003). The crosses are from Ganachaud and Wunsch 2003. The stream-function units are Sv.

Figure 9: Global ocean northward heat transport in petawatts. Observationally-based estimates are shown from the NCAR-NCEP reanalysis (stars; Kalney et al. 1996), the ECMWF reanalysis (circles; Gibson et al. 1997) and estimates with error bars by Ganachaud and Wunsch (2003; boxes) along with model estimates from ESM2M (red) and ESM2G (green).

Figure 10: Climatological seasonal cycle of integrated sea ice extent in the Northern (Figure 9A) and Southern (Figure 9B) hemisphere for an observationally based estimate from the National Snow and Ice Data Centerusing a reference period of 1979 through 2000 (Fetterer etal, 2009; http://nsidc.org/data/g02135.html; black) compared with the ESM2M (red) and ESM2G (green) preindustrial runs.

Figure 11: Climatological minimum (top) and maximum (bottom) mixed layer depths (m) using the Levitus 0.125 density criterion (Levitus, 1982). In each case, the left column is an observational estimate using temperature (Locarnini et al. 2010) and salinity (Antonov et al.

2010) from World Ocean Atlas 2009. The middle (ESM2M) and right (ESM2G) columns are the model derived diagnostics of the actively mixing layer. On the model maps are plotted the bias, correlation coefficient and standard error between the model and observationally based fields.

Figure 12: Maps of the vertical gradient in potential density referenced to the surface ($d\sigma_\theta/dz$; kg m^{-3} km^{-1}) for World Ocean Atlas 2009 (WOA09; Locarnini et al. 2010), ESM2M, and ESM2G at 300 m (top: A, B, C, respectively), 600 m (middle: D, E, F, respectively) and with depth along 160W (bottom: G, H, I, respectively). For the bottom panels, contours of potential density surfaces that signify the bottom of mode waters in the southern ocean (σ_θ = 27.2) and in the North Pacific (σ_θ = 26.7) for WOA09 (G), ESM2M (H) and ESM2G (I) are overlain for reference. Note the non-linear scale that goes linearly between 0.1 to 1 kg m^{-3} km^{-1} to highlight the low stratification mode waters and then switches to a logarithmic scale beyond.

Figure 13: Maps of basin averaged ocean age tracer in the Atlantic and Pacific for ESM2M (A, D), ESM2G (B, E) and the difference of ESM2G minus ESM2G (C, F) averaged from years 1001-1100 of the simulations. In each case, contours of potential temperature are overlaid for ESM2M (red) and ESM2G (green). The bottom set of panels show average Pacific profiles between 40S and 40N for potential temperature (G) and Age (H) and Age versus potential temperature (I) for ESM2M (red) and ESM2G (green). Panel G also shows the observational estimate for potential temperature from World Ocean Atlas 2009 (Locarnini et al. 2010; solid) as well as the potential temperature with a constant 0.5C subtracted from it as a very crude proxy for expectation for actual preindustrial conditions.

Figure 14: Southern Ocean maps of zonally averaged ocean age tracer for ESM2M (A) and ESM2G (B) along with contours of potential density (σ_θ; black) and meridional overturning circulation (Sv; green).

Figure 1:

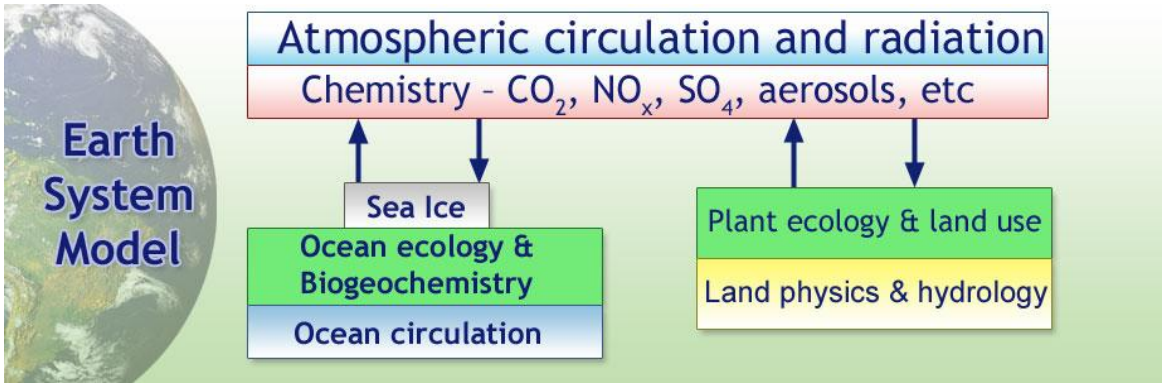
Earth System Model
Atmospheric circulation and radiation
Chemistry - CO_2, NO_x, SO_4, aerosols, etc
Sea Ice
Ocean ecology & Biogeochemistry
Ocean circulation
Plant ecology & land use
Land physics & hydrology

Figure 2:

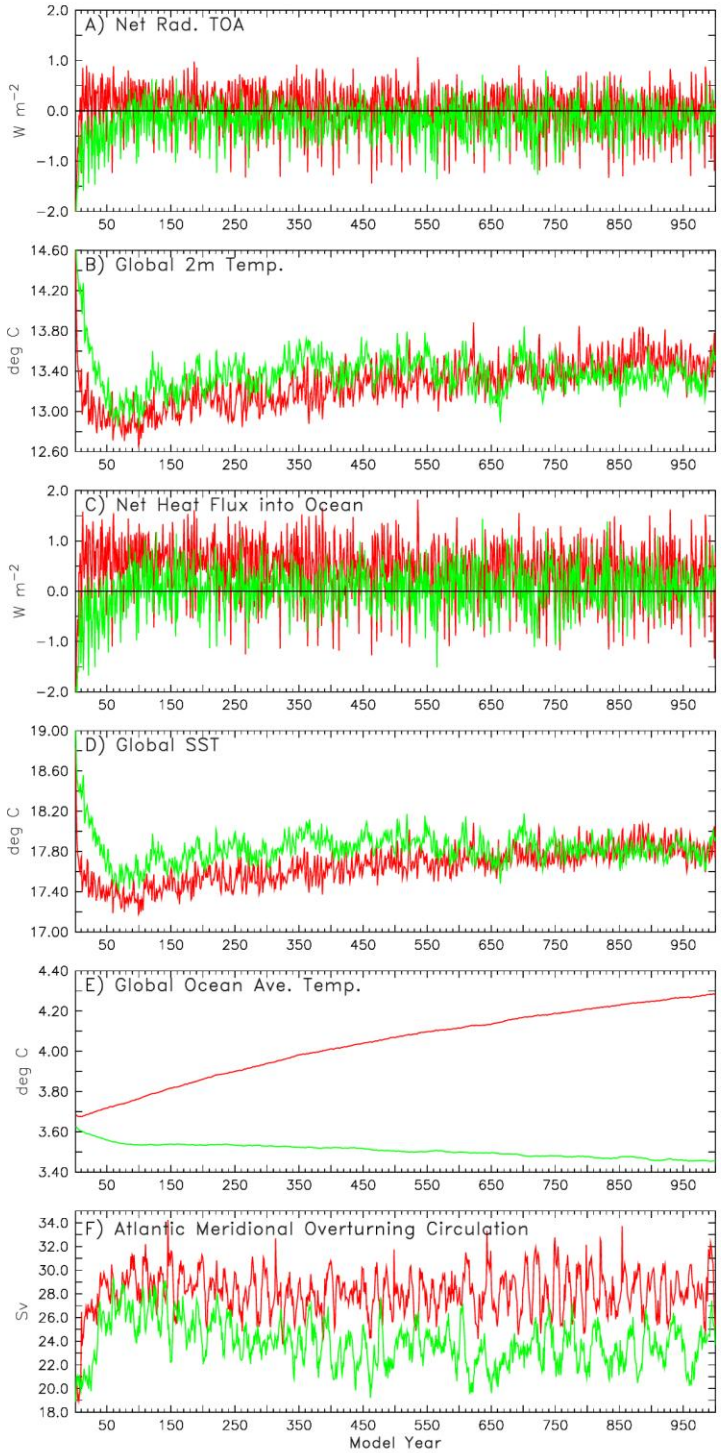
A) Net Rad. TOA
W m^{-2}
B) Global 2m Temp.
deg C
C) Net Heat Flux into Ocean
W m^{-2}
D) Global SST
deg C
E) Global Ocean Ave. Temp.
deg C
F) Atlantic Meridional Overturning Circulation
Sv
Model Year

Figure 3:

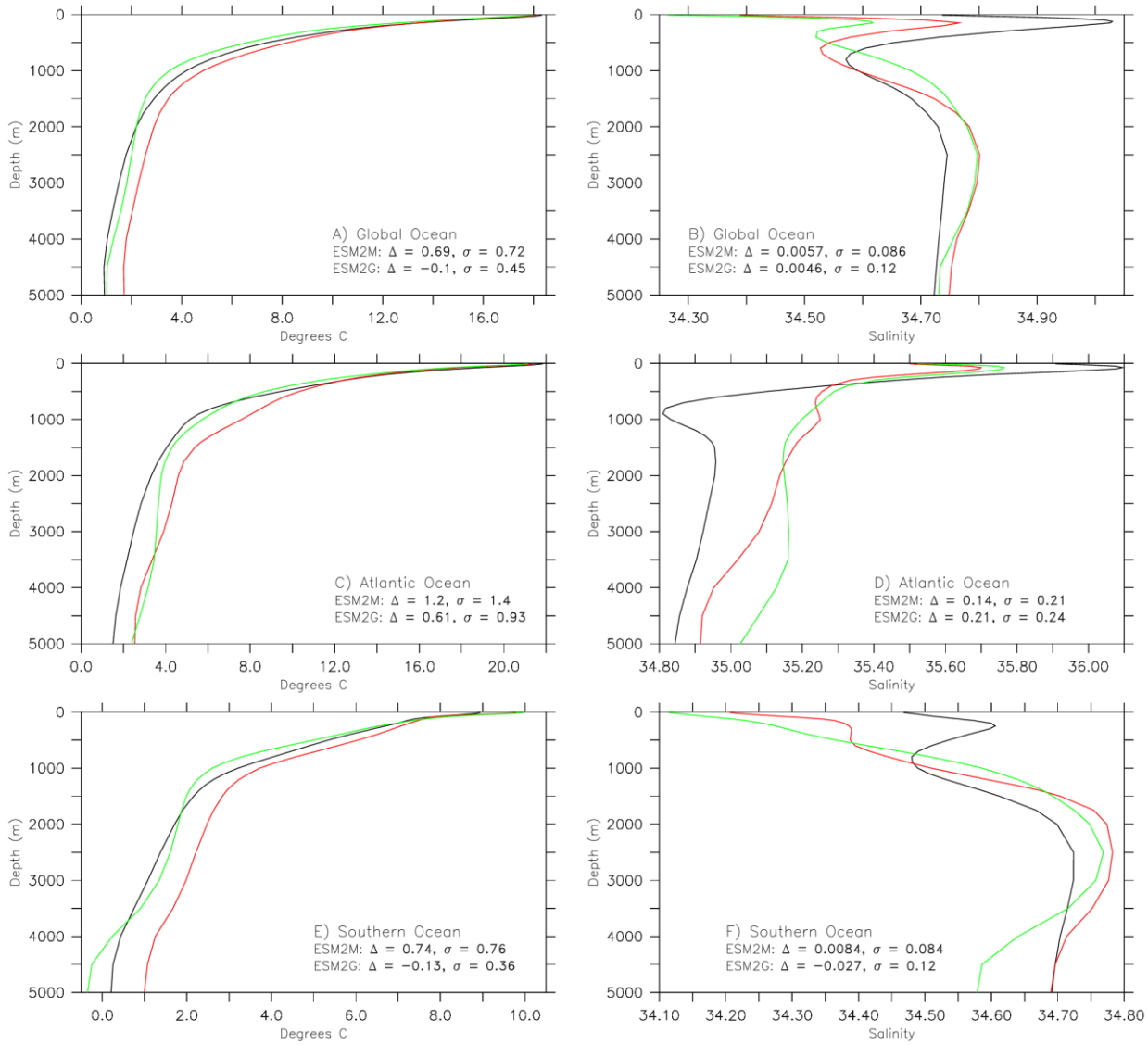
A) Global Ocean
ESM2M: Δ = 0.69, σ = 0.72
ESM2G: Δ = −0.1, σ = 0.45
B) Global Ocean
ESM2M: Δ = 0.0057, σ = 0.086
ESM2G: Δ = 0.0046, σ = 0.12
C) Atlantic Ocean
ESM2M: Δ = 1.2, σ = 1.4
ESM2G: Δ = 0.61, σ = 0.93
D) Atlantic Ocean
ESM2M: Δ = 0.14, σ = 0.21
ESM2G: Δ = 0.21, σ = 0.24
E) Southern Ocean
ESM2M: Δ = 0.74, σ = 0.76
ESM2G: Δ = −0.13, σ = 0.36
F) Southern Ocean
ESM2M: Δ = 0.0084, σ = 0.084
ESM2G: Δ = −0.027, σ = 0.12
Depth (m)
Degrees C
Salinity

Figure 4:

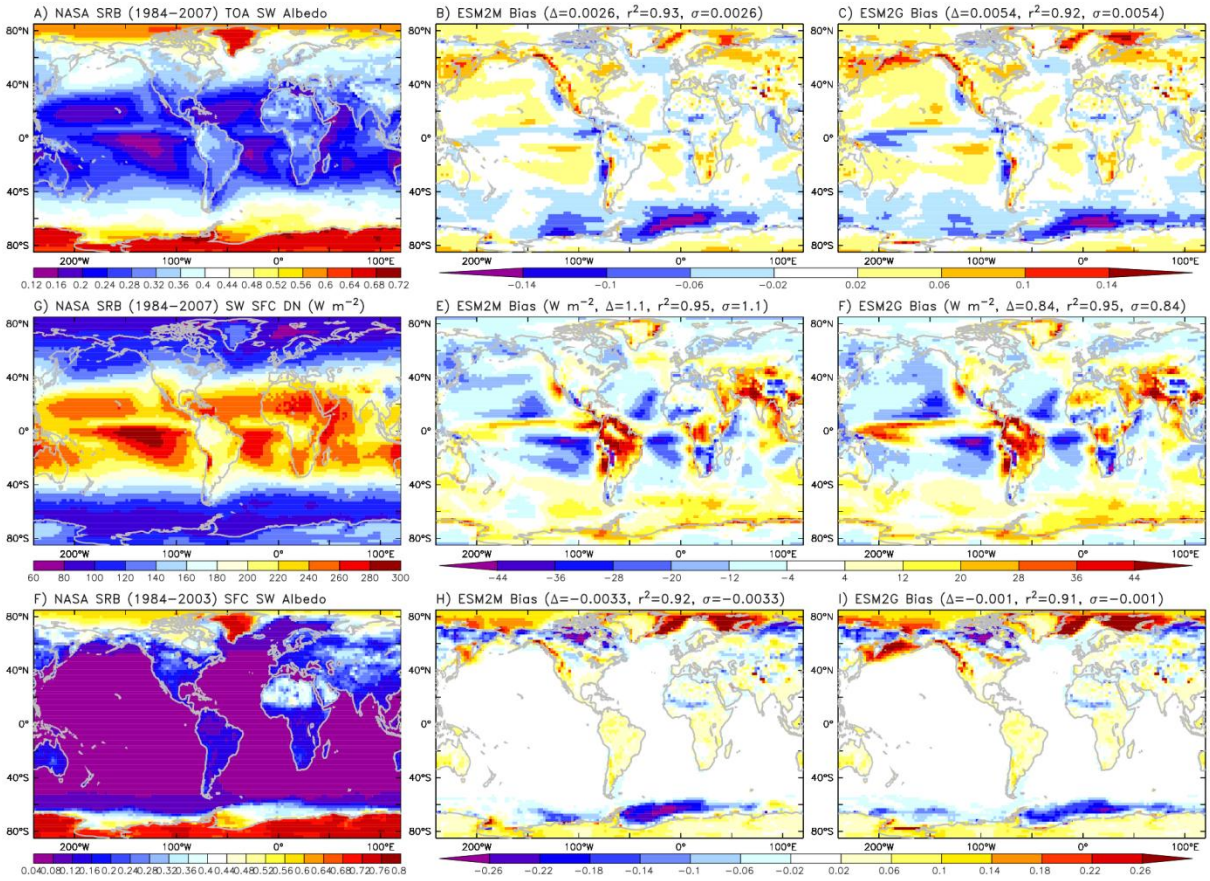
A) NASA SRB (1984–2007) TOA SW Albedo
B) ESM2M Bias (Δ=0.0026, r²=0.93, σ=0.0026)
C) ESM2G Bias (Δ=0.0054, r²=0.92, σ=0.0054)
G) NASA SRB (1984–2007) SW SFC DN (W m⁻²)
E) ESM2M Bias (W m⁻², Δ=1.1, r²=0.95, σ=1.1)
F) ESM2G Bias (W m⁻², Δ=0.84, r²=0.95, σ=0.84)
F) NASA SRB (1984–2003) SFC SW Albedo
H) ESM2M Bias (Δ=−0.0033, r²=0.92, σ=−0.0033)
I) ESM2G Bias (Δ=−0.001, r²=0.91, σ=−0.001)
80°N
40°N
0°
40°S
80°S
200°W
100°W
0°
100°E

Figure 5:

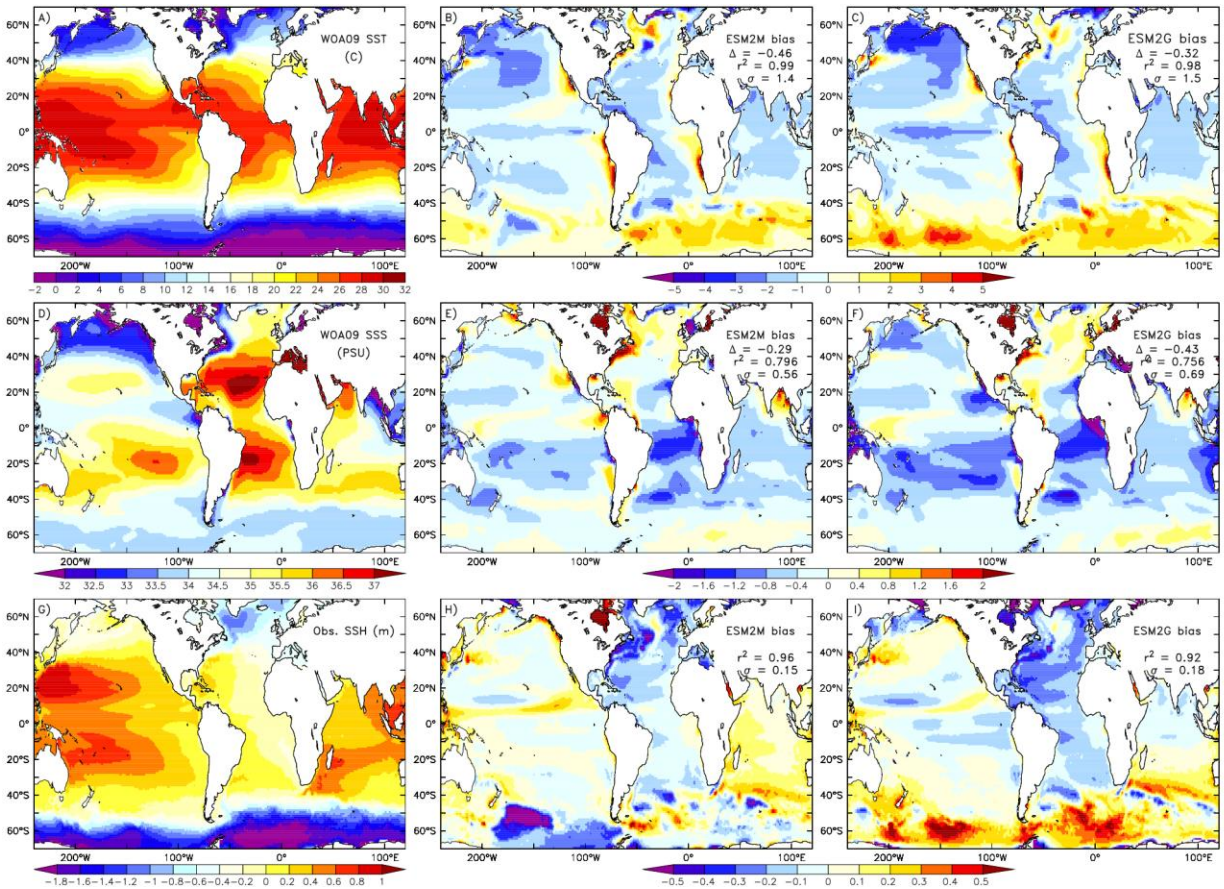
A)
WOA09 SST
(C)
B)
ESM2M bias
Δ = −0.46
r² = 0.99
σ = 1.4
C)
ESM2G bias
Δ = −0.32
r² = 0.98
σ = 1.5
D)
WOA09 SSS
(PSU)
E)
ESM2M bias
Δ = −0.29
r² = 0.796
σ = 0.56
F)
ESM2G bias
Δ = −0.43
r² = 0.756
σ = 0.69
G)
Obs. SSH (m)
H)
ESM2M bias
r² = 0.96
σ = 0.15
I)
ESM2G bias
r² = 0.92
σ = 0.18
60°N
40°N
20°N
0°
20°S
40°S
60°S
200°W
100°W
0°
100°E
−2 0 2 4 6 8 10 12 14 16 18 20 22 24 26 28 30 32
−5 −4 −3 −2 −1 0 1 2 3 4 5
32 32.5 33 33.5 34 34.5 35 35.5 36 36.5 37
−2 −1.6 −1.2 −0.8 −0.4 0 0.4 0.8 1.2 1.6 2
−1.8 −1.6 −1.4 −1.2 −1 −0.8 −0.6 −0.4 −0.2 0 0.2 0.4 0.6 0.8 1
−0.5 −0.4 −0.3 −0.2 −0.1 0 0.1 0.2 0.3 0.4 0.5

Figure 6:

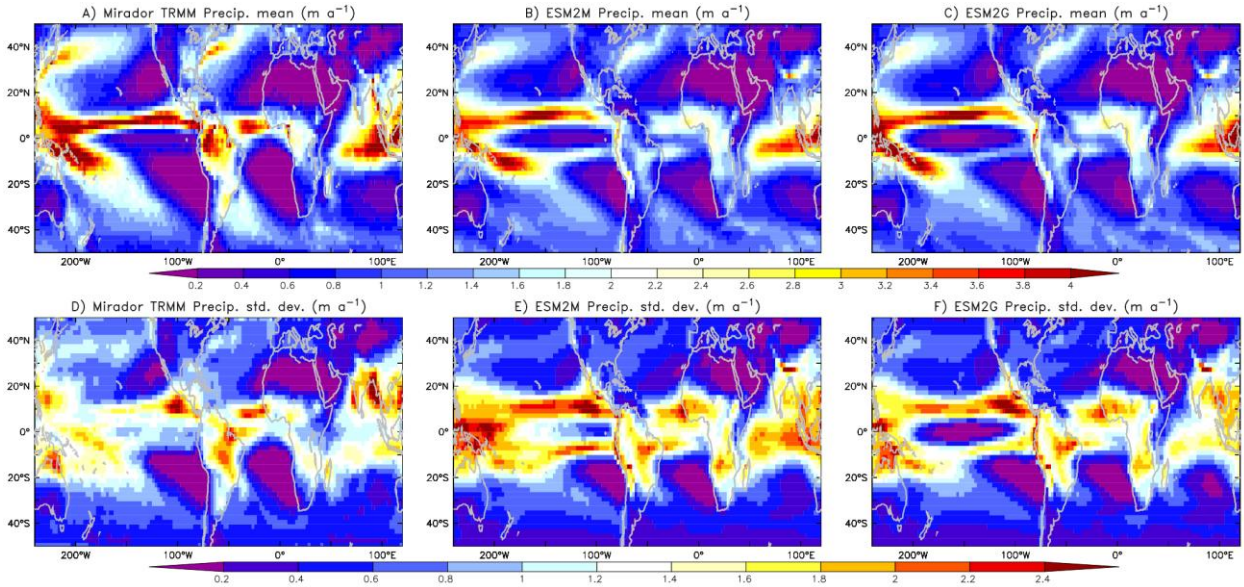
A) Mirador TRMM Precip. mean (m a^{-1})
B) ESM2M Precip. mean (m a^{-1})
C) ESM2G Precip. mean (m a^{-1})
D) Mirador TRMM Precip. std. dev. (m a^{-1})
E) ESM2M Precip. std. dev. (m a^{-1})
F) ESM2G Precip. std. dev. (m a^{-1})
40°N
20°N
0°
20°S
40°S
200°W
100°W
0°
100°E
0.2 0.4 0.6 0.8 1 1.2 1.4 1.6 1.8 2 2.2 2.4 2.6 2.8 3 3.2 3.4 3.6 3.8 4
0.2 0.4 0.6 0.8 1 1.2 1.4 1.6 1.8 2 2.2 2.4

Figure 7:

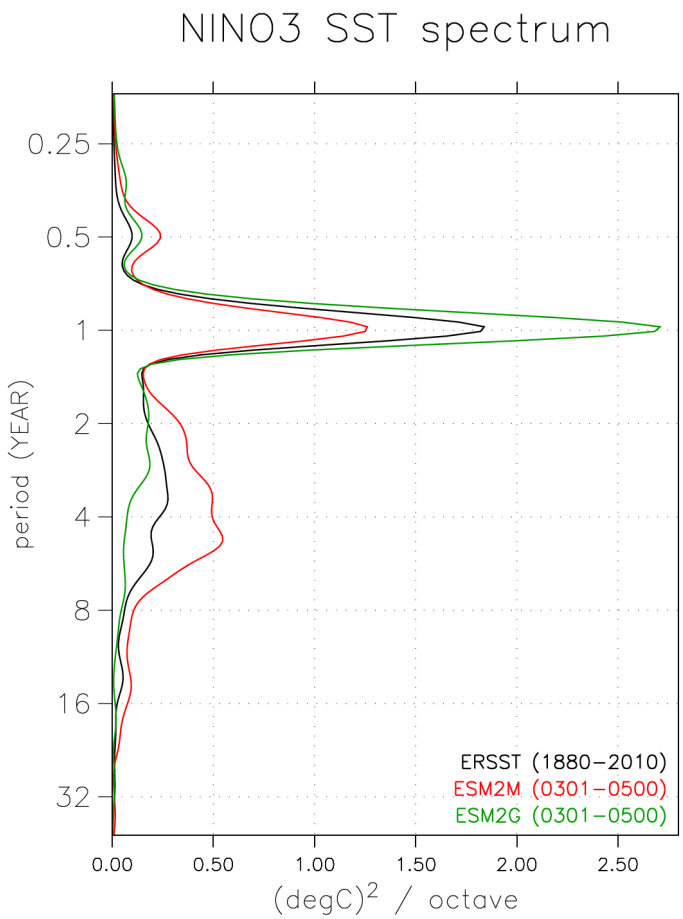
NINO3 SST spectrum
period (YEAR)
0.25
0.5
1
2
4
8
16
32
0.00
0.50
1.00
1.50
2.00
2.50
(degC)^2 / octave
ERSST (1880–2010)
ESM2M (0301–0500)
ESM2G (0301–0500)

Figure 8:

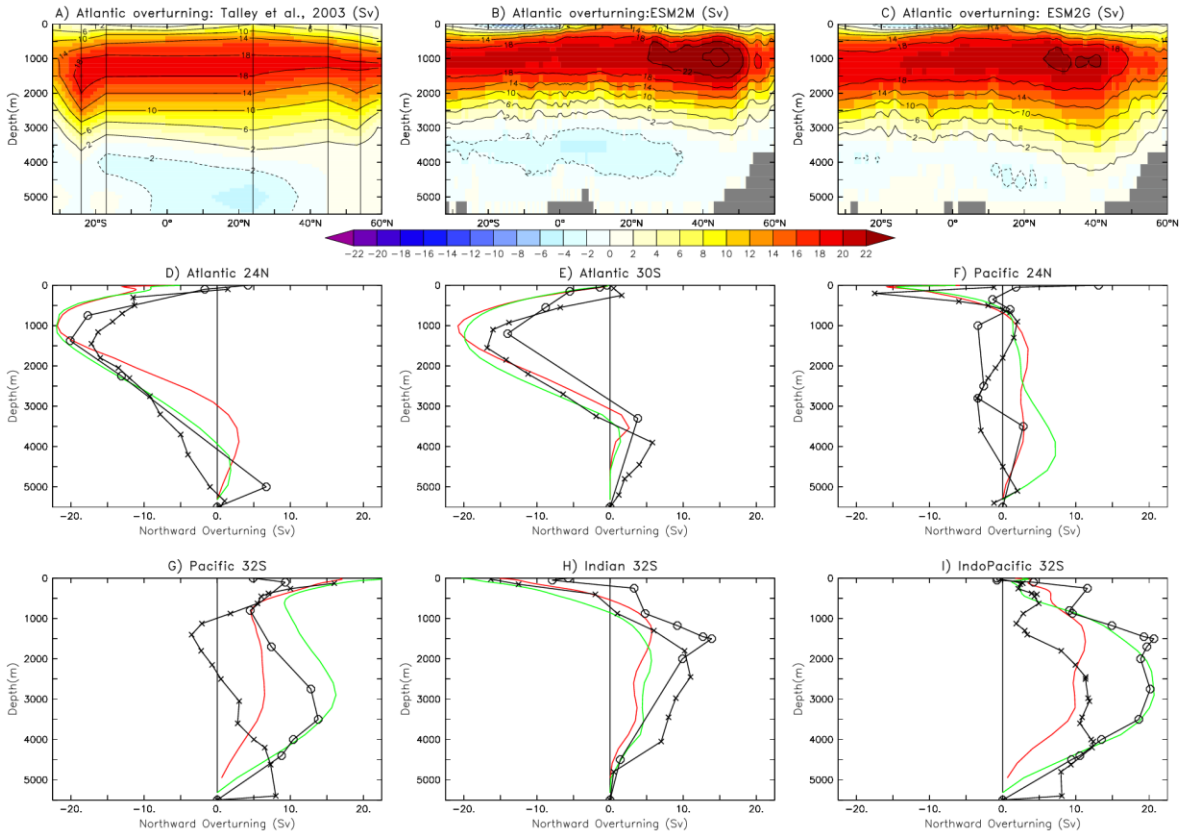
A) Atlantic overturning: Talley et al., 2003 (Sv)
B) Atlantic overturning:ESM2M (Sv)
C) Atlantic overturning: ESM2G (Sv)
D) Atlantic 24N
E) Atlantic 30S
F) Pacific 24N
G) Pacific 32S
H) Indian 32S
I) IndoPacific 32S
Depth(m)
Northward Overturning (Sv)
20°S
0°
20°N
40°N
60°N

Figure 9:

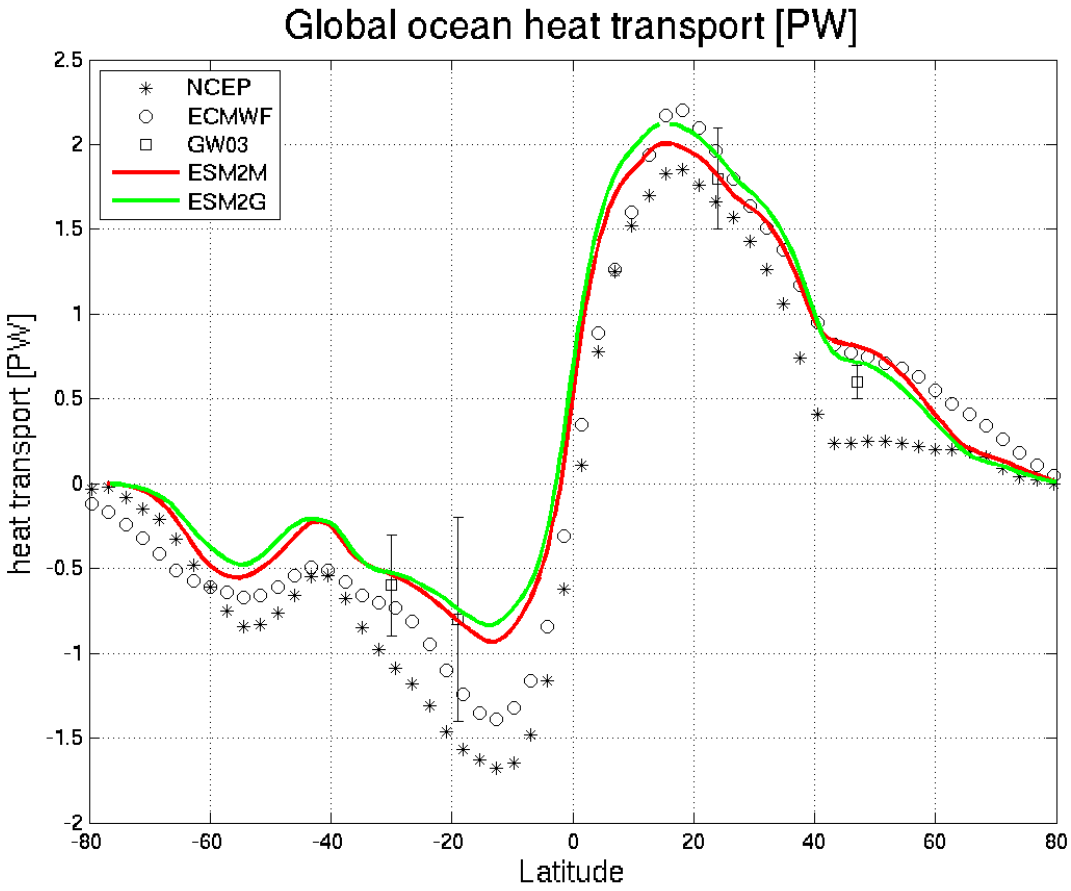
Global ocean heat transport [PW]
NCEP
ECMWF
GW03
ESM2M
ESM2G
heat transport [PW]
Latitude
2.5
2
1.5
1
0.5
0
-0.5
-1
-1.5
-2
-80
-60
-40
-20
0
20
40
60
80

Figure 10:

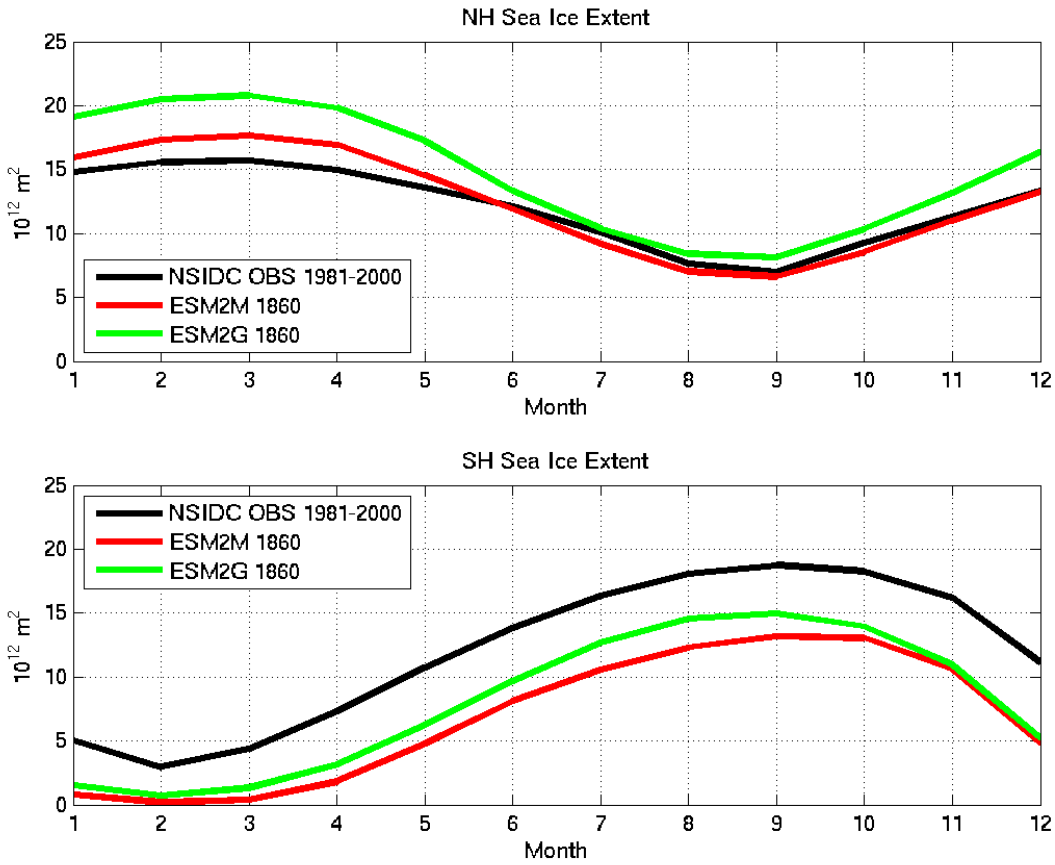
NH Sea Ice Extent
10^{12} m^2
Month
NSIDC OBS 1981-2000
ESM2M 1860
ESM2G 1860
SH Sea Ice Extent
10^{12} m^2
Month
NSIDC OBS 1981-2000
ESM2M 1860
ESM2G 1860

Figure 11:

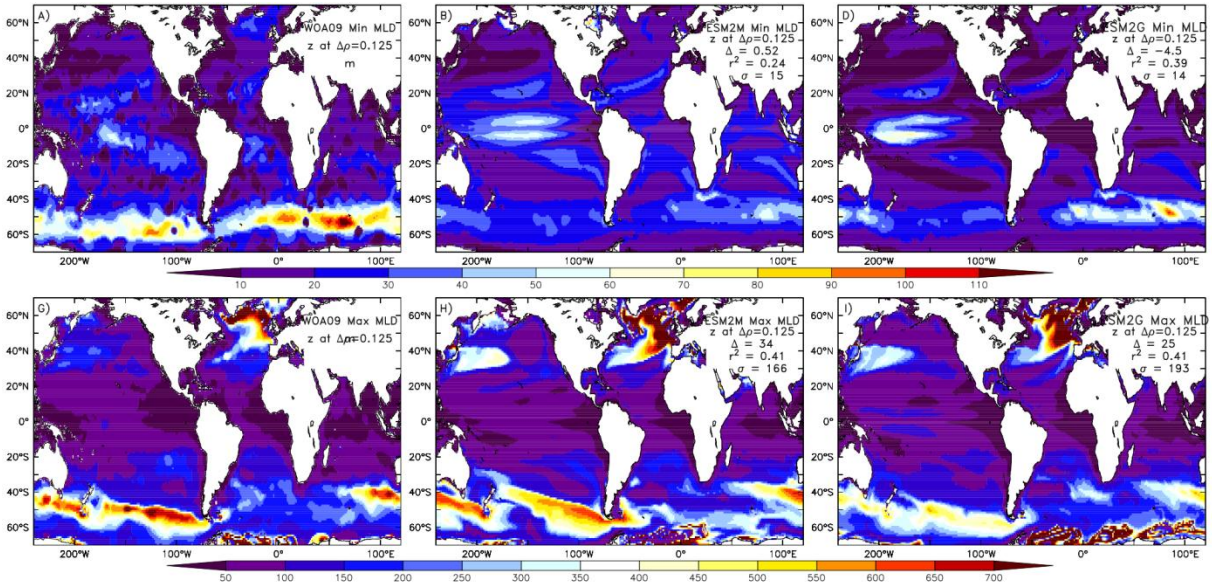
A)
WOA09 Min MLD
z at Δρ=0.125
m
B)
ESM2M Min MLD
z at Δρ=0.125
Δ = 0.52
r² = 0.24
σ = 15
D)
ESM2G Min MLD
z at Δρ=0.125
Δ = −4.5
r² = 0.39
σ = 14
G)
WOA09 Max MLD
z at Δρ=0.125
H)
ESM2M Max MLD
z at Δρ=0.125
Δ = 34
r² = 0.41
σ = 166
I)
ESM2G Max MLD
z at Δρ=0.125
Δ = 25
r² = 0.41
σ = 193
60°N
40°N
20°N
0°
20°S
40°S
60°S
200°W
100°W
0°
100°E
10 20 30 40 50 60 70 80 90 100 110
50 100 150 200 250 300 350 400 450 500 550 600 650 700

Figure 12:

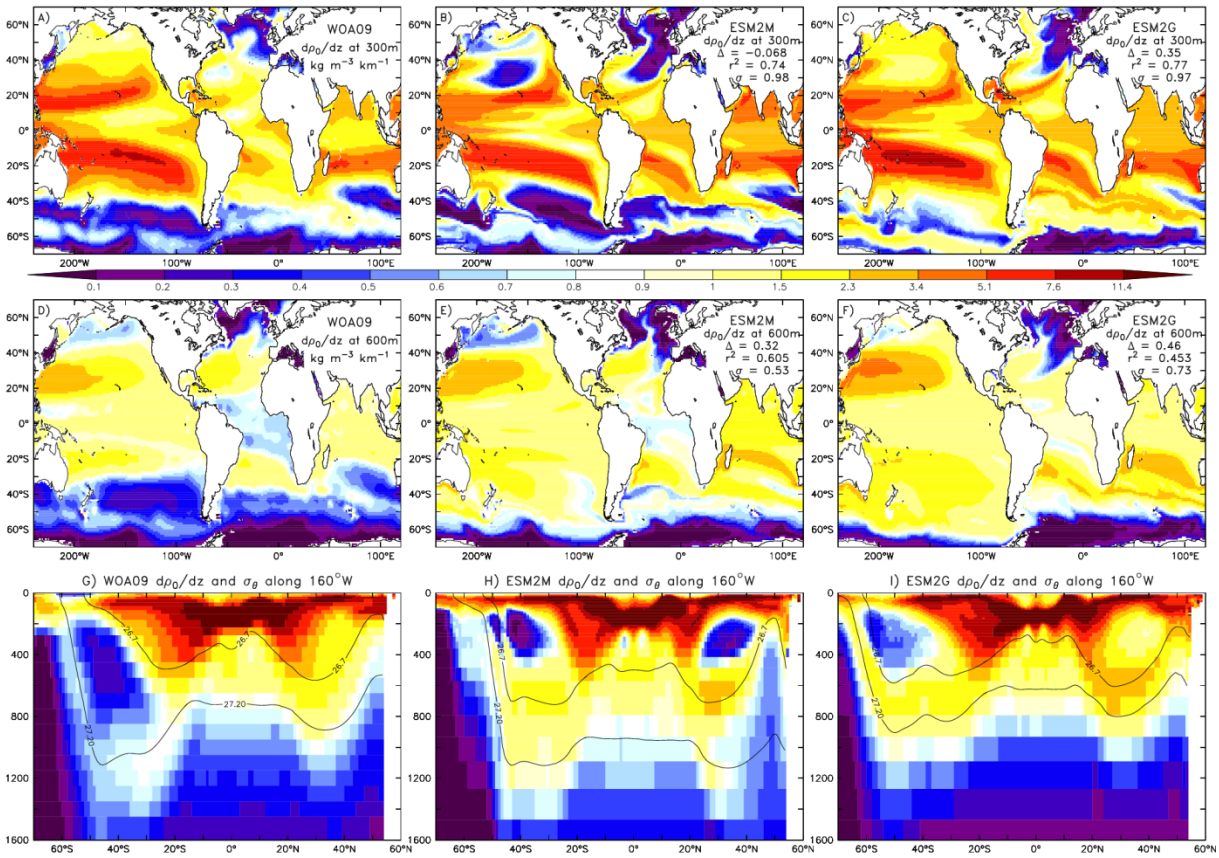
A)
WOA09
$d\rho_0/dz$ at 300m
kg m^{-3} km^{-1}
B)
ESM2M
$d\rho_0/dz$ at 300m
Δ = −0.068
r^2 = 0.74
σ = 0.98
C)
ESM2G
$d\rho_0/dz$ at 300m
Δ = 0.35
r^2 = 0.77
σ = 0.97
D)
WOA09
$d\rho_0/dz$ at 600m
kg m^{-3} km^{-1}
E)
ESM2M
$d\rho_0/dz$ at 600m
Δ = 0.32
r^2 = 0.605
σ = 0.53
F)
ESM2G
$d\rho_0/dz$ at 600m
Δ = 0.46
r^2 = 0.453
σ = 0.73
0.1 0.2 0.3 0.4 0.5 0.6 0.7 0.8 0.9 1 1.5 2.3 3.4 5.1 7.6 11.4
G) WOA09 $d\rho_0/dz$ and σ_θ along 160°W
H) ESM2M $d\rho_0/dz$ and σ_θ along 160°W
I) ESM2G $d\rho_0/dz$ and σ_θ along 160°W
27.20

Figure 13:

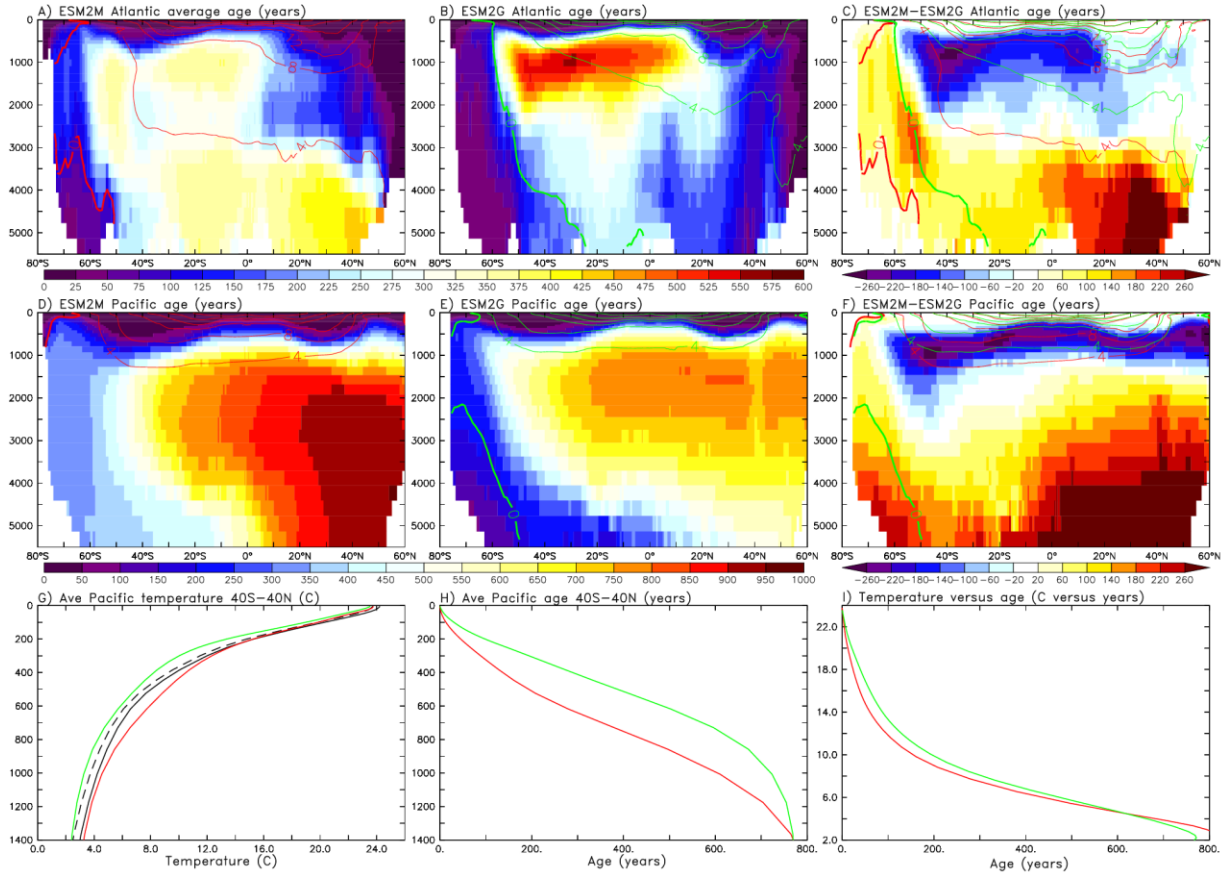
A) ESM2M Atlantic average age (years)
B) ESM2G Atlantic age (years)
C) ESM2M−ESM2G Atlantic age (years)
D) ESM2M Pacific age (years)
E) ESM2G Pacific age (years)
F) ESM2M−ESM2G Pacific age (years)
G) Ave Pacific temperature 40S−40N (C)
H) Ave Pacific age 40S−40N (years)
I) Temperature versus age (C versus years)
Temperature (C)
Age (years)
Age (years)

Figure 14:

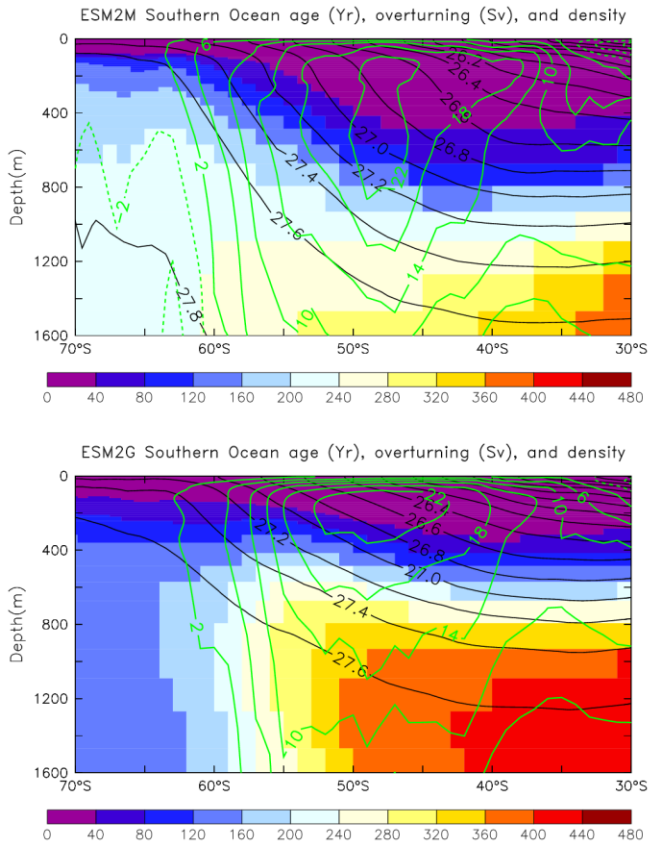
ESM2M Southern Ocean age (Yr), overturning (Sv), and density
Depth(m)
0
400
800
1200
1600
70°S
60°S
50°S
40°S
30°S
0 40 80 120 160 200 240 280 320 360 400 440 480
ESM2G Southern Ocean age (Yr), overturning (Sv), and density
Depth(m)
0
400
800
1200
1600
70°S
60°S
50°S
40°S
30°S
0 40 80 120 160 200 240 280 320 360 400 440 480